Bias Characterization of CrIS Radiances at 399 Selected Channels with Respect to NWP Model Simulations

X. Li[1,2] and X. Zou[2*]

[1]Jiangsu Research Institute of Meteorological Sciences, Jiangsu Meteorological Bureau, Nanjing, China

[2]Earth System Science Interdisciplinary Center, University of Maryland, College Park, Maryland, USA

Atmospheric Research

Submitted on January, 2017

Revised on April, 2017

*Corresponding author: Dr. X. Zou, Earth System Science Interdisciplinary Center, University of Maryland, College Park, MD 20740-3823, USA. Email: xzou1@umd.edu. Phone: 301-405-1532.

Abstract

The Cross-track Infrared Sounder (CrIS) on board the Suomi National Polar-Orbiting Partnership (S-NPP) satellite is a hyperspectral Fourier Transform Spectrometer. In this study, biases of the 399 channels used in numerical weather prediction applications are characterized based on the differences between CrIS observations and model simulations in clear-sky conditions over ocean. The Visible Infrared Imaging Radiometer Suite (VIIRS) cloud mask is used for selecting CrIS clear-sky data. The global mean biases are within ±1 K for most channels (more than 390). Biases for the channels not affected by trace gases other than water vapor in long-wave infrared (LWIR), middle-wave infrared (MWIR) and short-wave infrared (SWIR) bands vary from about -0.5 to 0.3 K, -0.2 to 0.8 K, and -0.1 to 0.9 K, respectively. The scan-angle variations of biases are less than ±0.4 K for all channels. The MWIR sounding channels have larger biases in middle and high latitudes than the tropics, which might be associated with latitudinal differences of water vapor variability. The SWIR CO_2 channels are affected by nonlocal thermodynamic equilibrium (NLTE) in the upper stratosphere and the window channels could be affected by the sun glint effect, both of which are considered in model simulations. Biases of the NLTE affected channels during daytime are found to be 0.5-1 K higher than nighttime. The SWIR window channels have colder biases at Field of Regards (FORs) 6-15 than the other scan positions due to the sun glint effect.

1. Introduction

Hyperspectral infrared sounders measure the earth radiation over thousands of channels, from which accurate atmospheric temperature and humidity profiles can be deduced at high vertical resolutions (Goldberg et al. 2003; Strow et al. 2003; Pougatchev et al. 2009). The Atmospheric Infrared Sounder (AIRS) (Aumann et al. 2003) flying on the NASA EOS Aqua satellite and the Infrared Atmospheric Sounding Interferometer (IASI) (Klaes et al. 2007) on board the MetOp-series satellites have provided more than 10 years of such infrared measurements at 2378 and 8461 spectral channels, respectively. Earlier infrared instruments, such as High Infrared Radiance sounders (HIRS), had no more than 20 channels. With the advances in computer technologies, the resolutions of global numerical weather prediction (NWP) models had increased to meso-scales and storm scales. The fine-scale vertical atmospheric structural information contained in hyperspectral infrared sounding data will contribute to improving short-range and medium-range weather forecast skills. Based on model simulations of IASI, Prunet *et al.* (1998) showed that an assimilation of IASI data generated an analyzed field with realistic baroclinic atmospheric structures that is important for constraining forecast errors. McNally et al. (2006) found out that a single AIRS assimilation outperformed a single HIRS assimilation due to a finer vertical scale of the analysis increments of temperature and humidity produced by assimilating AIRS hyperspectral infrared observations.

On 28 October 2011, Suomi National Polar-Orbiting Partnership (S-NPP), the first satellite in the series of next-generation U.S. satellites in Joint Polar Satellite

System (JPSS), was launched into a sun-synchronous orbit at a nominal altitude of 824 km. The equator cross local time of S-NPP is 13:30 at its ascending node. The Cross-track Infrared Sounder (CrIS) on board the S-NPP satellite is a hyperspectral Fourier Transform Spectrometer. It has 1305 spectral channels to cover long-wave infrared (LWIR), middle-wave infrared (MWIR) and short-wave infrared (SWIR) bands. CrIS is a Michelson interferometer like IASI and performs a similar spectral coverage as AIRS, which is a grating spectrometer. Since the launch of S-NPP, continuous well-planned efforts have been made on the radiometric calibration (Tobin et al. 2013), the spectral calibration and validation (Strow et al. 2013) and the geometric assessment (Wang et al. 2013). Therefore, reliable CrIS radiance data are made available for the purposes of weather monitoring, climate application and data assimilation.

For CrIS data assimilation, the use of large volume of data is not efficient and inter-channel error correlations must be avoided. A proper selection of hyperspectral infrared channels, also known as channel thinning, is necessary. Inheriting from the previous channel selection methodology of AIRS (Fourrie and Thepaut 2003) and IASI (Collard 2007), a subset of 399 CrIS channels was selected for NWP by the National Oceanic and Atmospheric Administration/National Environmental Satellite and Information Service (NOAA/NESDIS) channel selection methodology. These 399 CrIS channels selected for NWP applications consist of 184 LWIR, 128 MWIR and 87 SWIR channels. Gambacorta and Barnet (2013) demonstrated that these 399 channels fully represent the total atmospheric variability contained in the full

1305-channel spectrum.

Another important issue for CrIS hyperspectral infrared data assimilation is the bias correction. Since the theory of data assimilation is based on the assumption that background and observation errors are unbiased Gaussian, satellite instrumental biases that often have geographical and scan angle dependences need to be properly quantified and removed before assimilation (Dee 2005, Auligne et al. 2007). A widely adopted approach for estimating the instrumental bias is based on the departures of satellite radiances from model background fields, assuming the background as an unbiased reference. For most operational satellite infrared instruments (e.g., HIRS, AIRS and IASI), as described in Saunders et al. (2013), the radiance biases and their variations with time, geographic location, satellite zenith angle and scene temperature were characterized and monitored daily. The scan-dependent and geographic-dependent biases can be modeled in the variational data assimilation through a bias correction scheme (Eyre 1992; Harris and Kelly 2001; Auligne et al. 2007). The quality of CrIS data in clear-sky conditions over ocean was assessed by comparison with the Radiative Transfer for TIROS Operational Vertical Sounder (RTTOV) model simulated observations derived from the NWP model fields at the Met Office (Smith et al., 2015). However, Smith et al. (2015) mainly focused on the global mean biases and their standard deviations for a portion of LWIR CO_2 channels and MWIR H_2O channels that are daily assimilated in the NWP system of Met Office. For further assessments, the CrIS biases with respect to scan positions and latitudes need to be evaluated in all the three LWIR, MWIR and SWIR bands. Yin (2016) evaluated the bias differences of the short-wave channels near 4.3 μm with and without activating the nonlocal thermal equilibrium correction scheme in the Community Radiative Transfer Model (CRTM). However, this research was limited with very little data within a regional domain and a short time period. This study aims at obtaining more objective and representative bias characteristics for all the 399 CrIS channels selected by NOAA/NESDIS for NWP on a global scale for a much larger data samples.

To avoid the uncertainty of cloudy radiance simulation, only clear-sky CrIS pixels are used in the bias estimation. The S-NPP Visible Infrared Imager Radiometer Suite (VIIRS) cloud mask (CM) is employed for finding the clear CrIS field of views (FOVs), which is different from the stand-alone cloud detection algorithm (e.g. McNally and Watts, 2003) within NWP assimilation system that was used in the study by Smith et al. (2015). As evaluated in Kopp et al. (2014), the VIIRS CM can detect clear and cloudy pixels at VIIRS resolution with an agreement to the collocated Cloud-Aerosol Lidar with Orthogonal Polarization (CALIOP) data as high as 90%. Such an accuracy of cloud detection is comparable to other cloud masks such as the Aqua Moderate Resolution Imaging Spectroradiometer (MODIS) cloud detection. Besides, due to the existence of biases of land surface skin temperatures in global model fields (Trigo et al. 2015) and uncertainties of land surface emissivity assigned in radiative transfer models (RTMs), simulations of surface-sensitive infrared channels are much less accurate over land than over ocean (Zou et al. 2016). For this reason, only the clear-sky data pixels over ocean are used for CrIS bias estimation. It is worth mentioning that the biases estimated based on the observation (O) minus simulation (B) (i.e. O-B) differences include the biases related to inaccurate instrument calibration, RTM errors (e.g. inadequate model assumptions, errors in spectroscopic database), systematic errors in the NWP background field, and some remaining cloud-contaminated data that a clear-sky data selection scheme fails to identify.

The rest of this paper is organized as follows: Section 2 briefly describes the observed CrIS radiance observations and numerical simulations. The methodology for calculating clear fraction for each CrIS FOV using VIIRS CM products and the process in determining the clear-sky CrIS pixels is provided in section 3. Section 4.1-4.3 presents the numerical results of CrIS global mean biases, including their scan and latitudinal dependences, based on CRTM simulations. Impacts of RTM on CrIS radiance biases are illustrated by comparing the O-B biases between two most popularly used RTMs (i.e. CRTM and RTTOV) in section 4.4. Conclusions and discussions are summarized in section 5.

2. Data Description

2.1 CrIS Observations

In this study, CrIS normal spectral resolution data containing 1305 channels are used. CrIS measures interferograms to obtain infrared radiance in LWIR, MWIR and SWIR, which cover the spectral ranges of 650-1095 cm^{-1}, 1210-1750 cm^{-1} and 2155-2550 cm^{-1} at a spectral interval of 0.625 cm^{-1}, 1.25 cm^{-1} and 2.5 cm^{-1}, respectively. Figure 1 shows the brightness temperatures and weighting function (WF) peaks of the 399 channels calculated from a clear-sky tropical atmospheric profile with 51 vertical levels. The channel numbers covering the CrIS spectrum for the 399 channels are listed in Table 1. We highlight different absorption bands in Fig. 1, according to the work by Gambacorta and Barnet (2013). The 184 LWIR channels mainly cover carbon dioxide, water vapor, window and ozone bands (Fig. 1a). The carbon dioxide and water vapor LWIR channels are sensitive to atmospheric temperature and humidity fields. Most of the 128 selected MWIR channels are influenced by the absorption of water vapor and other trace gases (Fig. 1b). Meanwhile, the SWIR bands are composed of 87 channels (Fig. 1c), including the strong carbon dioxide absorbing bands near 4.3 μm (2325 cm^{-1}) which are affected by the so-called nonlocal thermodynamic equilibrium (NLTE) (Chen et al. 2013) and the window channels.

Figure 2 displays the vertical distributions of normalized weighting functions (WFs) for the 399 channels (Figs. 2a-c) and an example showing the variation of WF with respect to scan position and pressure for LWIR channel 36 (716.25 cm^{-1}) (Fig. 2d). Both LWIR (Fig. 2a) and SWIR (Fig. 2c) bands contain stratosphere sounding, troposphere sounding and surface channels, while channels in the MWIR band are mainly located in the troposphere (Fig. 2b). As a cross-track sounder, CrIS finishes one single scan within eight seconds, containing 30 Fields of Regard (FORs) of earth scene views. Each FOR is comprised of a 3×3 array of FOVs, which have a size around 14 km at nadir. In this study, the center FOV in each FOR is employed for the bias estimation. Along the cross-track direction, the satellite zenith angles of the 30

FORs vary from -48.3° to +48.3°, with a approximate interval of 3.3°. As shown in Fig. 2d, the WF peak of LWIR channel 36 is located at about 565 hPa, with an upward shift away from the nadir position. Since the FORs with larger scan angles experience longer optical paths, their WF peaks are higher than that at the nadir.

The CrIS Sensor Data Record (SDR) contains calibrated and geolocated radiance spectra transformed from directly measured interferograms. The hamming apodization function are applied to the unapodize SDR data, with a three-point filter {a, 1-2a, a} of running mean, where a = 0.23 (Han et al .2013). After the apodization, the brightness temperatures for the 399 CrIS channels are calculated from radiances data using Planck's blackbody radiation law. The brightness temperatures are used in this study.

2.2 Model Simulations

This study employs mostly the CRTM (Weng 2007; Han et al. 2007) version 2.2.3 as the forward radiative transfer model for generating model simulations of the CrIS brightness temperatures. The transmittance model coefficients for H_2O, O_3, CO_2, CH_4, CO and N_2O for CRTM are trained on Line-By-Line Radiative Transfer Model (LBLRTM) (Saunders et al. 2007). RTTOV (Saunders et al. 1999) version 11.2 is also employed to illustrate an impact of RTMs on bias estimation. The transmittance coefficients for H_2O, O_3, CO_2, CH_4, CO and N_2O for RTTOV are from the v9 predictor files of Hocking et al. (2013).

The European Center for Medium range Weather Forecasting (ECMWF) analyses valid at 0300 UTC, 0900 UTC, 1500 UTC and 2100 UTC, respectively, with a horizontal resolution of 0.25×0.25 degrees and 91 vertical model levels are used as the input to CRTM and RTTOV. The model level top of ECMWF analyses is at 0.01 hPa. In order to obtain the simulated brightness temperature at CrIS observed pixel locations and times, a bilinear interpolation and a linear interpolation are performed on the ECMWF analyses in the horizontal and temporal dimensions, respectively. The input variables to CRTM and RTTOV include the three-dimensional atmospheric temperature, water vapor mixing ratio, pressure as well as the two-dimensional surface variables of surface skin temperature, wind speed and wind direction. The ozone mixing ratio from the ECMWF analyses and a constant carbon dioxide mixing ratio of 390 ppmv are used for both CRTM and RTTOV simulations. The reference profiles for other trace gases (i.e. CH_4, CO and N_2O) within CRTM and RTTOV are used. The concentrations of CH_4 and N_2O in RTTOV are slightly higher than those in CRTM, especially in the troposphere, and the CO concentration in RTTOV is nearly the same as CRTM. It should be reminded that a lack of real profiles for trace gases may alias into biases for those channels sensitive to CH_4, CO and N_2O (see Fig. 1).

Two months of data, covering the period from June 30 to July 31 and November 30 to December 31, 2015, are employed for calculating the differences of brightness temperatures between CrIS observations and ECMWF/CRTM simulations in section 4.1-4.3. In order to mimimize the impacts of clouds, uncertainty in land surface emissivity model and background land surface temperature on bias estimation, this study only use data over ocean under clear-sky conditions. The International Geosphere-Biosphere Programme (IGBP) land type data set is used for identifying the oceanic data. Among all the CrIS pixels labeled by “water” in the land type, further efforts are made to exclude the pixels within 50 km from coastlines to remove those mixed pixels with land. Since the oceanic area in polar region is largely covered by sea ice, the O-B data within the latitudes of 55S and 55N are considered for the bias estimation. In addition, bias results estimated by RTTOV are compared with those by CRTM in section 4.4.

3. Determination of Clear-sky CrIS Data by Collocated VIIRS Cloud Mask

This study employs VIIRS CM products for determining whether or not a given CrIS FOV is clear. VIIRS onboard Suomi-NPP satellite consists of 22 bands, covering 16 moderate resolution bands (“M” bands), 5 imaging resolution bands (“I” bands) and one day-night band. Inheriting the MODIS CM algorithm (Ackerman et al. 1998), the VIIRS CM algorithm (Hutchison et al., 2005; Kopp et al. 2013) makes full use of VIIRS “M” and “I” bands and includes eleven/seven cloud detection tests (e.g. reflectance test, brightness temperature difference test, etc.) for determining daytime/nighttime clouds. Taking all the cloud detection tests into consideration, the cloud probability at each VIIRS pixel can be estimated. Based on the probability, the following four cloud confidences are classified: confidently cloudy, probably cloudy, probably clear and confidently clear, along with four quality flags: high, medium, low and poor. The final VIIRS CM products are provided with the spatial resolution of 750 m and 1.5 km at nadir and at the scan edge, respectively. Besides, the VIIRS CM also serves as an intermediate product for the VIIRS downstream Environmental Data Records (EDR), such as cloud top height and cloud top temperature products.

In order to obtain a clear fraction for the center FOV of each CrIS FOR, VIIRS pixels are collocated with CrIS FOVs. Based on the geolocation information, the footprints of CrIS FOVs can be accurately computed (Wang et al. 2013). For each CrIS FOV, VIIRS CM data with the quality flags of high or medium that locate within the FOV footprint are used to calculate the clear fraction as the ratio of confidently and probably clear VIIRS pixels to the total number of all the VIIRS pixels within the CrIS FOV. Figure 3 displays the global contribution of clear fractions at CrIS pixels, together with the VIIRS observed reflectance at the "M3" visible band with the wavelength of 0.486 μm on 17 December 2015. The global distribution of clear fractions shows reasonable features (Fig. 3a), with the high clear fractions corresponding to low reflectance (Fig. 3b). With the purpose of obtaining a reliable bias estimation, the CrIS pixels with 100% clear fraction are selected to determine the clear-sky CrIS pixels in this study.

Figure 4 provides a global distribution of total clear-sky CrIS data counts over ocean within $5^{o}x5^{o}$ grid boxes for the sampling period of two months (Fig. 4a), as well as the data counts with respect to latitudes and scan positions (Fig. 4b). Most regions have more than 100 clear-sky CrIS pixels, except for some small areas near the equator or high latitudes (Fig. 4a). As expected, more clear pixels are observed in the extratropical regions (Fig. 4b). The sufficiency of clear CrIS data count ensures a reliable estimation of CrIS biases and their latitudinal and scan variations.

4. CrIS Bias Characteristics

In satellite data assimilation, both the observations (O) and model simulations

(B) are assumed unbiased. Therefore, biases in observations (μ^o) and model simulations (μ^b) must be subtracted for the expression of the differences between observations and model simulations that appear in data assimilation formula:

$$(O-\mu^o)-(B-\mu^b) \quad (1)$$

with the biases being defined as

$$\mu^o = \overline{O-T}\ , \quad \mu^b = \overline{B-T} \quad (2)$$

where "T" represents the true atmosphere. An estimate of μ^o and μ^b, based on (2) requires the truth, which is never known.

A simple re-organization of the terms in the expression (1) gives (Weng et al., 2012):

$$(O-\mu^o)-(B-\mu^b)=O-B-(\mu^o+\mu^b) \quad (3)$$

Therefore, for data assimilation, it is fortunate that we only need to estimate the sum $\mu^o+\mu^b$ instead of μ^o and μ^b, respectively. Taking the mean of the term on the right-hand-side over many samples, we obtain

$$\mu^o + \mu^b = \overline{O-B} \quad (4)$$

The statistical evaluation of observation minus background (O-B) differences could include not only the instrument characteristics, but also systematic errors in NWP model background or forward radiative model. Impacts of the possible cloud-contaminated data are minimized by selecting those CrIS data with collocated clear VIIRS cloud mask.

4.1 LWIR Channels

Figure 5 presents the global mean biases of brightness temperatures at FORs 1-2, FORs 15-16 and FORs 29-30 within 55S-55N for LWIR bands. The global mean biases of the LWIR sounding channels 1-73 located in the CO_2 band and CO_2/H_2O (666.25-755.625 cm^{-1}) are within [-0.5 K, 0.3 K] and [-1.0 K, -0.4 K] below and above 50-hPa altitude (see Fig. 1a), respectively. The large negative biases are found for LWIR channels 2-5 that peak above 50 hPa, which could be associated with model errors of temperature analysis (Saunders et al., 2013). For the surface channels 91-128 (823.75-980 cm^{-1}), the global mean biases vary from -0.3 K to 0.1 K. Besides, the channels 141-179 (1010-1066.25 cm^{-1}) are affected by both the mixing ratio of stratospheric ozone and surface conditions. They are characterized by consistently positive biases and the largest bias is around 1 K. The differences of the global mean biases at different scan positions are within $\pm$0.3 K for all the LWIR channels.

As a cross-track sounder, the optical paths and the size of FOVs vary with the scan angles. These features lead to scan-dependent differences in the observed radiances as well as their biases. Figure 6a shows the biases of brightness temperatures for LWIR sounding channels 1-73 (666.25-755.625 cm^{-1}) (indicated by purple and green shaded regions in Fig. 1a) as functions of scan positions. In order to better illustrate the scan-dependent differences, the biases at each scan position are subtracted by the nadir bias, which is calculated by the averaged brightness temperatures at FORs 15 and 16. For the stratospheric CO_2 channels 6-20 (672.5-698.75 cm^{-1}) which peak below 50-hPa altitude, the biases increase with scan angle to about 0.2~0.3 K at the outmost scan positions. In comparison, for the CO_2/H_2O channels 28-73 (707.5-755.625 cm^{-1}) peak in the troposphere, the biases decrease with the scan angle to reach a value between -0.2 and -0.3 K. Such a pattern difference of scan biases between troposphere and stratosphere is probably related to a reverse scan variation of brightness temperatures (Fig. 6a). Channel 13 (689.375 cm^{-1}) (Fig. 6b) and channel 70 (752.5 cm^{-1}) (Fig. 6c) are selected to show such a difference of scan bias patterns between stratosphere and troposphere. Since the atmospheric temperature increase and decrease with altitudes in the stratosphere and troposphere, respectively, the observed brightness temperatures of stratospheric (Fig. 6b) and tropospheric (Fig. 6c) channels generally show upward curve and downward curve pattern, respectively. Although having similar scan patterns, the simulated brightness temperatures have smaller curvatures than those of observations. As a result, the O-B differences increase with scan angle in the stratosphere (Fig. 6b) and decrease with scan angle in the troposphere (Fig. 6c).

The latitudinal dependence of the biases and standard deviations of O-B brightness temperature differences for LWIR sounding channels 1-73 at all FORs are displayed in Fig. 7a. The latitudinal distributions of biases are distinctively different for the low stratospheric CO_2 channels 10-24 (686.25-702.5 cm^{-1}), high and middle tropospheric channels 28-36 (707.5-716.25 cm^{-1}) and low tropospheric channels 40-73 (724.375-755.625 cm^{-1}) (see Fig. 1a). Channels 10-24 primarily have negative biases with the largest negative biases in the tropics. Channels 28-36 have positive biases with the smallest biases (less than 0.15 K in magnitude) in the low latitudes and larger biases (~0.3 K) in the middle and high latitudes. For the low tropospheric channels 40-73, the biases are generally negative in the tropics and decreases in magnitude with latitude. The tropospheric channels 28-73 that are affected by the absorption of both CO_2 and H_2O have larger standard deviations than the stratospheric channels, especially in the tropical regions.

A possible cause for the bias differences between tropics and extratropics of LWIR CO_2 channels is the use of a fixed value of CO_2 concentration in model simulations. It is done so due to a lack of realistic CO_2 profiles from the ECMWF analysis fields. As discussed in Engelen and Bauer (2014), a real CO_2 concentration usually has higher values in the tropics than high latitudes (see Fig. 1 in Engelen and Bauer 2014). Therefore, a lack of a realistic latitudinal dependent CO_2 concentration in model simulation may result in a latitude-dependent bias for CO_2 channels. We conducted a sensitivity experiment in which the CO_2 concentration is 390 ppmv at 0^o, 380 ppmv at 90^o, and varies linearly with latitude in between. When comparing the bias results from this CO_2 sensitivity experiment with that from the fixed CO_2 experiment (Fig. 7b), it is found that reducing the CO_2 concentration increases the simulated brightness temperature due to a reduced CO_2 absorption. The CO_2 concentration at 55N (or 55S) in the sensitivity experiment is approximately -6 ppmv lower than the fixed value of 390 ppmv. The simulated brightness temperature for LWIR channels 36 (716.25 cm^{-1}) at 55N (or 55S) would be about 0.15 K warmer if the CO_2 concentration was reduced by about -6 ppmv than the control experiment. This would contribute to an additional bias of about -0.15 K. Such a latitudinal dependence of the biases due to a fixed CO_2 concentration specified in NWP data assimilation systems must be removed for the assimilation of CrIS LWIR CO_2

channels.

4.2 MWIR Channels

The global mean biases of brightness temperatures at FORs 1-2, FORs 15-16 and FORs 29-30 within 55S-55 N for the MWIR band is presented in Fig. 8. Water vapor is the primary absorbing constituent for all the MWIR bands. However, several other trace gases, such as CH_4 and SO_2, also affect the spectral band (1212.5-1387.5 cm^{-1}). It is seen that negative biases varying from about -0.2 K to -1.8 K are found for channels 185-227. For the channels 235-275, the global mean biases are within ±0.4 K. For the water vapor channels 280-312 (1400-1745 cm^{-1}), the global mean biases are generally positive except for channels 309-312 which are also slightly affected by the HNO_3 absorption. Several low-level channels (e.g. channel 296 and 304) have relatively large positive biases of more than 0.8 K. Furthermore, bias differences between the nadir and large scan positions are smaller than ±0.2 K except for the CH_4 channels.

The scan biases for MWIR channels 185-312 are presented in Fig. 9a. The scan biases for the MWIR H_2O channels 280-312 (1400-1745 cm^{-1}) (indicated by cyan shaded region in Fig. 1b) are within the range of ±0.2 K from 55S to 55N, which are smaller than those in the LWIR channels (Fig. 6). An asymmetric feature is found for the biases of the upper- and middle-tropospheric channels 298-312. The biases in the rightmost scan (FOR 30) are about 0.2 K less than those in the leftmost scan (FOR 1) for channels 298-303. Such an asymmetric scan bias feature can be found in the monthly means of both July and December (figures omitted). The exact mean differences of biases between FORs 1 and 30 for the MWIR channels 185-312 are provided in Fig. 9b, in which the mean values of the brightness temperature observations of different channels are indicated in colored dots. A notable asymmetric scan bias (more than 0.15 K) is found to be more significant for high-level channels with lower brightness temperatures (i.e. less than 240 K). For other MWIR channels (e.g. channels 195-285) which peak at low levels (Fig. 1b) and have higher observed brightness temperatures, the scan asymmetry of biases varies between 0.025 and 0.125 except for surface-sensitive channels 185-194. Since when the scene temperature is less than 240 K, CrIS observed brightness temperatures are more likely to be interfered by radiances from near field (e.g. spacecraft). In addition, the mean brightness temperatures from both observations and model simulations decrease with scan angle (Fig. 9c). In other words, brightness temperature observations at larger scan angle are lower and would be affected more by the near field side lobes. Given the fact that CrIS is located more to the right of the S-NPP spacecraft, the left side (FOR 1) of the scan seems to be affected more by the near field radiation than the right side of the scan (FOR 30), resulting a higher brightness temperature near FOR 1 than FOR 30 (see Fig. 9c).

Figure 10a displays the latitudinal dependence of biases for the MWIR channels 185-312. The biases for the MWIR H_2O channels 280-312 are found to be larger in higher latitudes than near the equator. The standard deviations of the O-B brightness temperature differences for these H_2O channels also increase from around 1 K near the tropics to more than 1.8 K in high latitudes. The latitudinal dependence of the biases is also found for other MWIR channels. This is found to be associated with a larger variability of water vapor in high latitudes. Different from the tropics where water vapor is abundant, regions of abundant water vapor in the middle and high latitudes are associated with cyclones and other weather systems, which propagate zonally and meridionally as these weather systems develop and decay (Fig. 11). Although having narrower and smaller regions (Fig. 11a-b), large 6-h differences of water vapor in high latitudes are more significant than the tropics. If we reduced the temporal collocation criteria between CrIS observations and background fields from ±3 h to ±1 h, both the biases and the standard deviations are decreased in middle and high latitudes and remain almost same in the tropics (Fig. 10b).

The scatter plots of O-B for MWIR channel 296 (1442.5 cm^{-1}) (see Fig. 2b) within the latitudinal bands of 35N~55N and 35S~55S shown in Fig. 12a further confirm that larger O-B differences are those when the observing times deviate further from the times of background fields at 0300, 0900, 1500 and 2100 UTC. Differences of brightness temperature between CrIS observations and model simulations in the tropics (Fig. 12b) are smaller and less affected by temporal interpolation. Impacts of temporal resolution on other CrIS channels that are not sensitive to water vapor are negligible (figure omitted).

4.3 SWIR Channels

Figure 13 presents the global mean biases of brightness temperatures at FORs 1-2, FORs 15-16 and FORs 29-30 within 55S-55N for the SWIR band. For the SWIR channels located in the CO/N_2O bands (2155-2195 cm^{-1}) and the Earth's surface

(2400-2540 cm^{-1}), the global mean biases are positive. The SO_2/CO_2 bands (2202.5-2262.5 cm^{-1}) are characterized by negative biases. Besides, the SWIR channels 358-378 (2292.5-2372.5 cm^{-1}) are affected by the NLTE emission. Although a fast NLTE radiance correction scheme was included in CRTM (Chen et al. 2013), the residual global mean biases for these NLTE channels can still be as high as 0.9 K. The SWIR biases have a scan symmetric feature. The larger the scan angles, the larger the biases.

SWIR channels are affected by solar radiation during the daytime. Because of the difficulties in accurately modeling reflected solar radiation, separating statistics between day and night is required for assimilation of SWIR channels. The scan-dependent biases for SWIR channels 358-399 (2292.5-2540 cm^{-1}) (indicated by orange and red shaded regions in Fig. 1c) are calculated separately during nighttime (Fig. 14a) and daytime (Fig. 14b). The nighttime scan variations of biases are generally smaller than daytime. The scan-dependent biases of the NLTE affected channels 358-378 increase positively with scan angle to a value around 0.3 K during daytime (Fig. 14b). A significant difference of the scan biases between daytime and nighttime are found for the window channels 388-399 (2400-2540 cm^{-1}). The daytime scan biases have a notable asymmetric distribution: positive for FORs 1-6 and 16-30 but negative for FORs 6-15.

It is well known that solar radiation could be reflected by sea surface into satellite sensor. The reflected solar radiation, which is also called sun glint, can affect the CrIS measurements of surface-sensitive channels located around 4 μm (2400-2540

cm^{-1}). In order to investigate whether the scan biases during daytime are related to the sun glint effect, we show in Fig. 15 the scan positions that could be affected by the sun glint (Fig. 15a) and the biases as a function of sun glint angle (Fig. 15b) for the SWIR surface channel 394 (2500 cm^{-1}) (see Fig. 2c). The sun glint angle θ_g is defined as the angle between the direction along which a satellite sensor views the surface and the direction of the reflected solar radiance (Chen et al., 2013):

$$\theta_g = \cos^{-1}[\cos(\theta_s)\cos(\theta_o) - \sin(\theta_s)\sin(\theta_o)\cos(\varphi_s - \varphi_o)] \quad (5)$$

where θ_s, θ_o, φ_s and φ_o are the sun zenith angle, satellite zenith angle, sun azimuth angle and satellite azimuth angle, respectively.

Since S-NPP crosses equator at 13:30 local time at its ascending node, the Sun is located to the west of the satellite nadir during daytime. Therefore, the scan positions located to the west of the nadir and east of the Sun could be affected by the sun glint as the sun glint angle is small. It is seen that the regions with sun glint angles being less than 30° and 10° take place at the scan positions 4-18 and 7-14, respectively (Fig. 15a). Meanwhile, when the sun glint angle is below 30 °, the bias decreases dramatically as the sun glint angle decreases (Fig. 15b). Since the bidirectional reflectance distribution function (BRDF) proposed by Breon (1993) was implemented in CRTM to fully consider the sun glint effect (Chen et al., 2013), the negative biases when the sun glint angles are small are probably caused by an overcorrection of the sun glint effect in CRTM.

The latitudinal biases for SWIR channels are presented separately for daytime and nighttime as well as for July and December (Fig. 16). To avoid the sun glint effect on SWIR window channels, all CrIS pixels with sun glint angles less than 30° during daytime are excluded. Notable differences are found between daytime biases (Figs. 16a and 16c) and nighttime biases (Figs. 16b and 16d), as well as the biases in July (Figs. 16a and 16b) and December (Figs. 16c and 16d). For the NLTE channels 358-378 (2292.5-2372.5 cm^{-1}), warmer biases are higher during the daytime than the nighttime of both months. The daytime biases exceed 1.0 (1.0 K-1.5 K) and the nighttime biases are below 1 K in the tropics in either July or December. Similar results were found for the biases of IASI and AIRS NLTE channels during daytime by Chen et al. (2013) and DeSouza-Machado et al. (2007), respectively. Besides, during the daytime, the NLTE channels in high latitudes have larger biases over the Southern Hemisphere (SH) than the Northern Hemisphere (NH) in July (Figs. 16a). As expected, the NH have larger biases than in the SH in high latitudes in December (Figs. 16c). As described in Chen et al. (2013), a simple NLTE correction in addition to the local thermal equilibrium (LTE) is applied in CRTM to consider the NLTE effect. The impacts of satellite zenith angle and solar zenith angle on the NLTE correction are accounted for by a linear weighted average of three predictors, for which the weighting coefficients are the regression coefficients that are obtained by using 48 diversified training profiles (Strow et al. 2003). Since the NLTE correction term is a function of solar zenith angle, the simulations of NLTE channels may have different behaviors at different solar zenith angles. As pointed out by Chen et al. (2013), large dependences of biases on solar zenith angles were presented when solar zenith angles are greater than 70°. Since the high latitudes of NH and SH have solar zenith angles larger than 70° in December and July (figure omitted), respectively, the larger positive biases in high latitudes may be caused by the large solar zenith angles. Besides, for the window channels 388-399 (2400-2540 cm^{-1}), smaller differences are found in the biases between July and December. Again, the daytime biases are generally higher than the nighttime biases.

4.4 Comparison of CrIS Biases Estimated by CRTM and RTTOV Simulations

Figure 17 compares the biases of CrIS brightness temperatures estimated by CRTM (black, same as Figs. 5, 8 and 13) and RTTOV (red), and differences of bias between CRTM and RTTOV (blue) for the 399 channels at nadir (FORs 15-16). The differences of simulated brightness temperatures between the two RTMs are less than ±0.2 K for LWIR CO_2 channels. The estimated biases for the surface channels in LWIR and SWIR bands show even more consistent results from these two RTMs. For MWIR channels that are mainly affected by H_2O, the RTTOV simulations are generally 0~0.2 K lower than CRTM simulations. However, simulation differences are significant in some MWIR channels that are sensitive to CH_4 and some SWIR channels that are sensitive to N_2O. As mentioned in section 2.2, the concentrations of CH_4 and N_2O in RTTOV are slightly higher than those in CRTM, especially in the troposphere (Fig. 18). For CH_4 and N_2O sensitive channels, it would lead to larger absorptions of radiation from the surface and low troposphere, resulting in lower simulated brightness temperatures in RTTOV (B_{RTTOV}) than those in CRTM (B_{CRTM}) (see blue curve in Fig. 17). In addition to CH_4 and N_2O concentration differences, the transmittance model coefficients are different between these two fast radiative transfer models (Saunders et al. 2007). Therefore, the differences of simulated brightness temperatures between CRTM and RTTOV for CH_4 and N_2O channels can be ascribed to both the differences in reference profiles and the differences in transmittance coefficients.

Figure 19 shows the mean differences of biases between the outmost scan positions (FORs 1-2) and the nadir (FORs 15-16) estimated by CRTM and RTTOV, respectively. The simulated largest scan differences are nearly the same for all 399 CrIS channels in terms of the signs. There are some small differences in magnitudes between the two models for LWIR window channels, CH_4 and N_2O sensitive channels, CO_2 SWIR channels and the highest wavenumber SWIR window channels.

5. Summary and Conclusions

This study estimates the bias characteristics of the 399 CrIS channels selected for NWP applications. Differences of brightness temperatures between CrIS observations and model simulations are used for the bias estimate. To exclude the uncertainty of model simulations of cloudy radiances and land surface emissivity, only clear-sky CrIS pixels over ocean are employed. For selection of CrIS clear-sky pixels, the VIIRS cloud mask products collocated with CrIS FOV are used for calculating the clear fractions on CrIS pixels. Only the data pixels with a 100% clear fraction are finally used in order to obtain a more reliable estimation. To obtain a sufficiently large data sample, clear-sky CrIS pixels are identified from a two-month period (i.e., 30 June to 31 July, November 30 to December 31) in 2015.

Overall, the estimated global mean biases for LWIR, MWIR and SWIR channels are within a reasonable range of ±1 K except for the channels that are affected by trace gases. The mean biases of LWIR channels are generally smaller than those of MWIR and SWIR channels. Biases of all channels have scan and latitudinal dependences. The scan variation of LWIR biases are mostly within ±0.3 K. Most LWIR channels have the smallest biases in the tropics and increase toward high latitudes. The latitudinal variation of LWIR biases are within the range of ±0.4 K. Besides, the tropospheric CO_2/H_2O LWIR channels have larger standard deviations than the stratospheric CO_2 LWIR channels, especially in the tropical regions.

For the MWIR H_2O channels 280-312 (1400-1745 cm^{-1}), the scan biases vary from -0.2 to 0.2 K. A small asymmetry is found in scan biases for the upper-level H_2O channels 298-312 at all latitudes. Furthermore, both the biases and standard deviations increase with the latitude. The 6 hours interval of the ECMWF analyses used in this study seemed too long for capturing the temporal variability of water vapor.

The biases of SWIR channels during daytime and nighttime are analyzed separately due to a possible impact of the sun glint effect on some of these channels. It is found that the scan positions FORs 6-15 are most affected by the sun glint. The SWIR biases of the surface-sensitive channels located around 4 μm (2400-2540 cm^{-1}) are colder at scan positions FORs 6-15 than other scan positions. The opposite sign of scan biases at FORs 6-15 to the remaining FORs come from those data pixels affected by the sun glint when the sun glint angles is smaller than 30°. A latitudinal dependence is found for the biases of those SWIR channels affected by the NLTE when the solar zenith angles are greater than 70°. For all the SWIR channels that are affected by the solar radiation, the biases are higher during daytime than nighttime.

The bias results calculated based on RTTOV simulations are compared with those from CRTM simulations. It is concluded that the biases for CO_2 as well as surface channels are less affected by the RTM errors. However, channels that are sensitive to water vapor or other trace gases, are more affected by RTM errors.

The 399 CrIS channels in LWIR, MWIR and SWIR bands selected for bias estimation in this study are input to the National Centers for Environmental Prediction (NCEP) unified Gridpoint Statistical Interpolation (GSI) analysis system (Wu *et al.*, 2002). A follow-on work on CrIS data assimilation is CrIS inter-channel error correlation. Impacts of CrIS data assimilation on global and regional forecasts can finally be assessed.

This study only estimated CrIS biases based on two months data set under clear-sky and oceanic conditions. It is worth reminding that a different CrIS data set (e.g. CrIS channels different from the 399 channels selected for this study, data over land) could be used in various NWP modeling systems. For examples, CrIS channels which peak at levels higher than the detected cloud top are remained (McNally and Watts 2003) in NWP assimilation systems. Also, surface-sensitive channels are used over land after proper skin temperature sensitivity checks. In some operational NWP systems, only a small portion (LWIR channels and several MWIR H_2O channels) of CrIS channels is currently assimilated. Other channels are used for monitoring purposes. NOAA is now disseminating a full spectral resolution (FSR) product with

0.625 cm^{-1} sampling over the whole spectrum. The FSR will be the nominal choice for CrIS to be onboard JPSS-1 in the future. A similar study will be carried out for these new datasets.

Acknowledgments and Disclaimers: This research work has been jointly supported by the NOAA JPSS Proving Ground and Risk Reduction (PGRR) Program (NA14NES4320003), the National Natural Science Foundation of China (Grant 41505052), and the Jiangsu Provincial Science and Technology Support Program (BE2013730, BE2015731). We thank the China Scholarship Council for their financial support toward the first author. The views expressed in this publication are those of the authors and do not necessarily represent those of NOAA. We also thank the editor and two anonymous reviewers for their valuable and constructive suggestions that significantly improved the science presentation of this manuscript.

References

Ackerman, S. A., K. I. Strabala, W. P. Menzel, R. A. Frey, C. C. Moeller, and L. E. Gumley, 1998: Discriminating clear sky from clouds with MODIS, *J. Geophys. Res.*, **103**, 32,141–32,157.

Auligné, T., A. P. McNally, and D. P. Dee, 2007: Adaptive bias correction for satellite data in a numerical weather prediction system. *Q. J. R. Meteorol. Soc.*, **133**(624), 631-642.

Aumann, H. H., and Coauthors, 2003: AIRS/AMSU/HSB on the Aqua mission: Design, science objectives, data products, and processing systems. *IEEE Trans. Geosci. Remote Sens.*, **41**(2), 253-264.

Breon, F. M., 1993: An analytical model for the cloud-free atmosphere/ocean system reflectance. *Remote Sens. Environ.*, 43, 179–192.

Chen, Y., Y. Han, P. V. Delst, and F. Weng, 2013: Assessment of shortwave infrared sea surface reflection and nonlocal thermodynamic equilibrium effects in the community radiative transfer model using IASI data, *J. Atmos. Oceanic Technol.*, 30, 2152–2160.

Collard, A. D., 2007: Selection of IASI channels for use in numerical weather prediction. *Q. J. R. Meteorol. Soc.*, **133**(629), 1977-1991.

Dee, D. P., 2005: Bias and data assimilation. *Q. J. R. Meteorol. Soc.*, **131**(613), 3323-3343.

DeSouza-Machado, S. G., L. L. Strow, S. E. Hannon, H. E. Motteler, M. Lopez-Puertas, B. Funke, and D. P. Edwards, 2007: Fast forward radiative transfer modeling of 4.3 um nonlocal thermodynamic equilibrium effects for infrared temperature sounders, *Geophys. Res. Lett.*, **34**, L01802, doi:10.1029/2006GL026684.

Engelen R. J., and P. Bauer, 2014: The use of variable CO_2 in the data assimilation of AIRS and IASI radiances. *Q. J. R. Meteorol. Soc.,* **140**: 958–965. DOI:10.1002/qj.919.Eyre, J. R., 1992: A bias correction scheme for simulated TOVS brightness temperatures. *European Centre for Medium-Range Weather Forecasts.*

Eyre J.R., 1992: A bias correction scheme for simulated TOVS brightness temperatures. *Technical Memorandum* 186, ECMWF, Reading, UK.

Fourri'e, N., and J. N. Thépaut, 2003: Evaluation of the AIRS near‐real‐time channel selection for application to numerical weather prediction. *Q. J. R. Meteorol. Soc.*, **129**(592), 2425-2439.

Gambacorta, A., and C. D. Barnet, 2013: Methodology and information content of the NOAA NESDIS operational channel selection for the Cross-track Infrared Sounder (CrIS), *IEEE Trans. Geosci. Remote Sens.*, **51**, 3207–3216.

Goldberg, M. D., Y. Qu, L. M. McMillin, W. Wolf, L. Zhou, and Divakarla, M., 2003: AIRS near-real-time products and algorithms in support of operational numerical weather prediction. *IEEE Trans. Geosci. Remote Sens.*, **41**(2), 379-389.

Han, Y., F. Weng, Q. Liu, and P. van Delst, 2007: A fast radiative transfer model for SSMIS upper atmosphere sounding channels. *J. Geophys. Res.*, **112**(D11), doi:10.1029/2006JD008208.

Han, Y., and coauthors, 2013: Suomi NPP Crls measurements, sensor data record algorithm, calibration and validation activities, and record data quality, *J. Geophys. Res. Atmos.*, **118**, 12,734-12,748. doi:10.1002/2013JD020344.

Harris, B. A., and G. Kelly, 2001: A satellite radiance-bias correction scheme for data assimilation. *Q. J. R. Meteorol. Soc.*, **127**(574), 1453-1468.

Hocking, J., P. J. Rayer, D. Rundle, R. W. Saunders, M. Matricardi, A. Geer, P. Brunel, and J. Vidot, 2013: RTTOV v11 Users Guide, NWP-SAF report, Met. *Office, UK*.

Hutchison, K. D., J. K. Roskovensky, J. M. Jackson, A. K. Heidinger, T. J. Kopp, M. J. Pavolonis, and R. Frey, 2005: Automated cloud detection and typing of data collected by the Visible Infrared Imager Radiometer Suite (VIIRS), *Int. J. Remote Sens.*, **20**, 4681–4706.

Klaes, K. D., and Coauthors, 2007: An introduction to the EUMETSAT polar system. *Bull. Amer. Meteor. Soc.*, **88**, 1085–1096.

Kopp, T. J., W. Thomas, A. K. Heidinger, D. Botambekov, R. A. Frey, K. D. Hutchison, B. D. Iisager, K. Brueske, and B. Reed (2014), The VIIRS Cloud Mask: Progress in the first year of S-NPP toward a common cloud detection scheme, *J. Geophys. Res. Atmos.*, **119**, 2441–2456, doi:10.1002/2013JD020458.

McNally, A. P., and P. D. Watts, 2003: A cloud detection algorithm for high spectral resolution infrared sounders. *Q. J. R. Meteorol. Soc.,* **129** (595), 3411-3423.

McNally, A. P., P. D. Watts, J. A Smith, R. Engelen, G. A. Kelly, J. N. Thépaut, and M. Matricardi, 2006: The assimilation of AIRS radiance data at ECMWF. *Q. J. R.*

Meteorol. Soc., **132** (616), 935-957.

Pougatchev, N., and Coauthors, 2009: IASI temperature and water vapor retrievals–error assessment and validation. *Atmos. Chem. Phys.*, **9**(17), 6453-6458.

Prunet, P., J. N. Thépaut, and V. Cassé, 1998: The information content of clear sky IASI radiances and their potential for numerical weather prediction. *Q. J. R. Meteorol. Soc.*, **124**(545), 211-241.

Saunders, R., M. Matricardi M., and P. Brunel, 1999: An improved fast radiative transfer model for assimilation of satellite radiance observations. *Q. J. R. Meteorol. Soc.*, **125**, 1407–1425.

Saunders, R., P. Rayer, P. Brunel, A. von Engeln, N. Bormann, L. Strow, S. Hannon, S. Heilliette, X. Liu, F. Miskolczi, Y. Han, G. Masiello, J.-L. Moncet, G. Uymin, V. Sherlock, and D. S. Turner, 2007: A comparison of radiative transfer models for simulating Atmospheric Infrared Sounder (AIRS) radiances. *J. Geoph. Res.*, **112**, D01S90, doi:10.1029/2006JD007088.

Saunders, R. W., T. A. Blackmore, B. Candy, P. N. Francis, and T. J. Hewison, 2013: Monitoring satellite radiance biases using NWP models. *IEEE Trans. Geosci. Remote Sens.*, **51**(3), 1124-1138.

Smith, A., N. Atkinson, W. Bell, and A. Doherty, 2015: An initial assessment of observations from the Suomi−NPP satellite: data from the Cross−track Infrared Sounder (CrIS). *Atmos. Sci. Let.*, **16**(3), 260-266.

Strow, L. L., S. E. Hannon, S. De Souza-Machado, H. E. Motteler, and D. Tobin, 2003:

An overview of the AIRS radiative transfer model. *IEEE Trans. Geosci. Remote Sens.*, **41**(2), 303-313.

Strow, L. L., H. Motteler, D. Tobin, H. Revercomb, S. Hannon, H. Buijs, J. Predina, L. Suwinski, and R. Glumb, 2013: Spectral calibration and validation of the Cross-track Infrared Sounder (CrIS) on the Suomi NPP satellite, *J. Geophys. Res. Atmos.*, **118**, 12,486 –12,496, doi:10.1002/2013JD020480.

Tobin, D., and Coauthors, 2013: Suomi-NPP CrIS radiometric calibration uncertainty, *J. Geophys. Res. Atmos.*, **118**, 10,589–10,600, doi:10.1002/jgrd.50809.

Trigo, I. F., S. Boussetta, P. Viterbo, G. Balsamo, A. Beljaars, and I. Sandu, 2015: Comparison of model land skin temperature with remotely sensed estimates and assessment of surface atmosphere coupling, *J. Geophys. Res. Atmos.*, **120**, 12,096–12,111, doi:10.1002/ 2015JD023812.

Wang, L., D. A. Tremblay, Y. Han, M. Esplin, D. E. Hagan, J. Predina, L. Suwinski, X. Jin, and Y. Chen (2013), Geolocation assessment for CrIS sensor data records, *J. Geophys. Res. Atmos.*, **118**, 12,690–12,704, doi:10.1002/2013JD020376.

Weng, F., 2007: Advances in radiative transfer modeling in support of satellite data assimilation. *J. Atmos. Sci.*, **64**, 3799-3807.

Weng, F., X. Zou, X. Wang, S. Yang, and M. D. Goldberg, 2012: Introduction to Suomi National Polar-Orbiting Partnership Advanced Technology Microwave Sounder for Numerical Weather Prediction and Tropical Cyclone Applications. *J. Geophys. Res. Atmos.*, **117**, doi: 10.1029/2012jd018144.

Wu, W. S., R. J. Purser, D. F. Parrish, 2002: Three-dimensional variational analysis with spatially inhomogeneous covariances. *Mon. Wea. Rev.* **130**, 2905-2916.

Yin, M., 2016: Bias characterization of CrIS shortwave temperature sounding channels using fast NLTE model and GFS forecast field, *J. Geophys. Res. Atmos.*, **121**, 1248–1263, doi:10.1002/2015JD023876.

Zou, X., X. Zhuge, and F. Weng, 2016: Characterization of bias of Advanced Himawari Imager infrared observations from NWP background simulations using CRTM and RTTOV. *J. Atmos. Oceanic Technol.*, **33**, 2553-2567. doi:10.1175/ JTECH-D-16-0105.1.

Table caption

Table.1: List of the subset of 399 CrIS channels selected by NOAA/NESDIS. The channel indices corresponding to the full spectrum are shown in brackets.

Figure caption

Fig. 1: Brightness temperatures (black) and weighting function peaks (blue) for (a) LWIR, (b) MWIR, (c) SWIR of the 399 CrIS channels used in NWP calculated by CRTM for a typical tropical atmosphere profile. The CO_2 channels of LWIR, CO_2/H_2O channels of LWIR, H_2O channels of MWIR, CO_2 channels of SWIR and window channels of SWIR are represented by purple, green, cyan, orange and red shaded regions, respectively. Other sensitive bands are indicated by grey regions.

Fig. 2: Normalized weighting functions for bands of: (a) LWIR, (b) MWIR and (c) SWIR. (d) Weighting functions with respect to scan positions and pressure for channel 36. The green, red, purple, blue, cyan, and orange lines in (a), (b) and (c) indicate the LWIR channels 13, 36 and 70, MWIR channels 296 and 303, and SWIR channel 394, respectively.

Fig. 3: (a) Spatial distributions of clear fractions within CrIS center FOV, and VIIRS reflectance observations at the M3 visible band centered at wavelength 0.486 μm on 17 December 2015.

Fig. 4: (a) Global distributions of clear-sky oceanic data counts within $5^o x 5^o$ grid boxes and (b) the data counts with respect to latitude and scan positions. The data with surface skin temperature below 273.15 K are excluded.

Fig. 5: The biases of brightness temperatures of LWIR channels for FORs 1-2 (blue line), FORs 15-16 (black line) and FORs 29-30 (red line).

Fig. 6: (a) Scan biases of brightness temperatures for LWIR channels of CO_2 and H_2O

absorption band averaged within 55S-55N. The nadir (FORs 15-16) bias is subtracted. The scan variations of mean observed brightness temperatures are shown (contours), with the mean brightness temperatures of FORs 15-16 subtracted. Scan variations of the mean brightness temperatures from observations (black curve) and model simulations (blue curve) and the O-B differences (red curve) for (b) LWIR channel 13 (689.375 cm^{-1}) and (c) channel 70 (752.5 cm^{-1}).

Fig. 7: Latitudinal dependences of biases and standard deviations of the O-B brightness temperature differences for LWIR channels of CO_2 and H_2O absorption bands with respect to latitude and channel number. (b) Latitudinal variations of the O-B differences (unit: K) for LWIR channel 36 (716.25 cm^{-1}) between the fixed CO_2 experiment (black curve) and a latitudinal varied CO_2 experiment (blue curve), and the $B_{varied\text{-}co2}$-$B_{fixed\text{-}co2}$ differences (red curve) with ($B_{varied\text{-}co2}$) and without ($B_{fixed\text{-}co2}$) varying CO_2 concentration with respect to latitudes.

Fig. 8: The biases of brightness temperatures of MWIR channels for FORs 1-2 (blue line), FORs 15-16 (black line) and FORs 29-30 (red line).

Fig. 9: (a) Scan variations of biases of brightness temperatures for MWIR channels within 55S-55N and (b) the mean differences of biases between FORs 1 and 30 (FOR 1 minus FOR 30) for MWIR channels 185-312 (dots). The nadir (FORs 15-16) bias is subtracted in (a). The mean values of the brightness temperature observations are indicated by colored the dots in (b). (c) Scan variations of the

mean brightness temperatures from observations (black curve) and model simulations (blue curve) and the differences (red curve) for MWIR channel 303 (1576.25 cm^{-1}).

Fig. 10: Latitudinal dependences of biases and standard deviations of the O-B brightness temperature differences for MWIR channels 185-312 with a collocation criteria of (a) ±3 h and (b) ±1 h.

Fig. 11: Specific humidity (unit: g kg^{-1}) around 500 hPa from ECMWF analysis at (a) 0300 and (b) 0900 UTC, 14 December 2015, and (c) their differences.

Fig. 12: Scatter plots of O-B of MWIR channel 296 (1442.5 cm^{-1}) for all the data in December within the latitudinal bands of (a) 35N~55N and 35S~55S and (b) 15S-15N. The variations of the bias and standard deviation are presented by red curve and vertical lines, respectively.

Fig. 13: The biases of brightness temperatures of SWIR channels for FORs 1-2 (blue line), FORs 15-16 (black line) and FORs 29-30 (red line).

Fig. 14: Biases of brightness temperature for SWIR channels with respect to scan and channel number at (a) nighttime and (b) daytime within the latitudes of 55S-55N. The nadir (FORs 15-16) bias is subtracted.

Fig. 15: Data counts (shaded in color) as (a) functions of sun glint angle (intv: 2^o) and scan positions and (b) functions of O-B (intv: 0.2 K) and sun glint angle (intv: 2^o) of SWIR channel 394 (2500 cm^{-1}) within the latitudes of 55S-55N at daytime. Variations of the global mean biases and the standard deviations with respect to sun glint angle are shown by black curve and vertical lines, respectively. The sun

glint angle of 30° is indicated by a grey line in both (a) and (b).

Fig. 16: Latitudinal dependences of biases and standard deviations of the O-B brightness temperature differences for SWIR channels in July during (a) daytime and (b) nighttime, and in December during (c) daytime and (d) nighttime.

Fig. 17: Biases of CrIS brightness temperatures estimated by CRTM (black, same as Figs. 5, 8 and 13) and RTTOV (red), and differences of bias between CRTM and RTTOV (blue) for the 399 channels at nadir (FORs 15-16). The CO_2 channels of LWIR, CO_2/H_2O channels of LWIR, H_2O channels of MWIR, CO_2 channels of SWIR and window channels of SWIR are indicated by purple, green, cyan, orange and red shadings, respectively. The channels sensitive to other trace gases are highlighted in grey shading.

Fig. 18: Reference profiles of CH_4 (left panel) and N_2O (right panel) concentrations within CRTM (red curve) and RTTOV (blue curve).

Fig. 19: Mean differences of biases between FORs 1-2 and FORs 15-16 (FORs 1-2 minus FORs 15-16) estimated by CRTM (black) and RTTOV (red).

Table.1: List of the subset of 399 CrIS channels selected by NOAA/NESDIS. The channel indices corresponding to the full spectrum are shown in brackets.

1(27)	2(28)	3(31)	4(32)	5(33)	6(37)	7(49)	8(51)	9(53)	10(59)
11(61)	12(63)	13(64)	14(65)	15(67)	16(69)	17(71)	18(73)	19(75)	20(79)
21(80)	22(81)	23(83)	24(85)	25(87)	26(88)	27(89)	28(93)	29(95)	30(96)
31(99)	32(101)	33(102)	34(104)	35(106)	36(107)	37(111)	38(113)	39(116)	40(120)
41(123)	42(124)	43(125)	44(126)	45(130)	46(132)	47(133)	48(136)	49(137)	50(138)
51(142)	52(143)	53(144)	54(145)	55(147)	56(148)	57(150)	58(151)	59(153)	60(154)
61(155)	62(157)	63(158)	64(159)	65(160)	66(161)	67(162)	68(163)	69(164)	70(165)
71(166)	72(168)	73(170)	74(171)	75(173)	76(175)	77(181)	78(183)	79(198)	80(208)
81(211)	82(216)	83(224)	84(228)	85(236)	86(238)	87(242)	88(248)	89(266)	90(268)
91(279)	92(283)	93(311)	94(317)	95(330)	96(333)	97(334)	98(338)	99(340)	100(341)
101(342)	102(349)	103(352)	104(358)	105(361)	106(364)	107(366)	108(367)	109(368)	110(378)
111(390)	112(391)	113(392)	114(394)	115(395)	116(396)	117(397)	118(398)	119(399)	120(404)
121(427)	122(447)	123(464)	124(473)	125(482)	126(484)	127(501)	128(529)	129(556)	130(557)
131(558)	132(560)	133(561)	134(562)	135(564)	136(565)	137(566)	138(569)	139(573)	140(574)
141(577)	142(580)	143(581)	144(584)	145(585)	146(587)	147(590)	148(591)	149(594)	150(597)
151(598)	152(601)	153(604)	154(607)	155(611)	156(614)	157(616)	158(617)	159(619)	160(622)
161(626)	162(628)	163(634)	164(637)	165(638)	166(640)	167(641)	168(642)	169(644)	170(646)
171(647)	172(650)	173(651)	174(652)	175(654)	176(655)	177(657)	178(659)	179(663)	180(667)
181(670)	182(707)	183(710)	184(713)	185(716)	186(730)	187(735)	188(736)	189(739)	190(743)
191(744)	192(746)	193(748)	194(751)	195(754)	196(755)	197(756)	198(757)	199(758)	200(760)
201(761)	202(762)	203(763)	204(766)	205(767)	206(768)	207(771)	208(772)	209(773)	210(776)
211(777)	212(778)	213(779)	214(780)	215(782)	216(783)	217(784)	218(785)	219(786)	220(787)
221(788)	222(789)	223(790)	224(791)	225(792)	226(794)	227(796)	228(798)	229(800)	230(802)
231(803)	232(804)	233(806)	234(807)	235(808)	236(809)	237(811)	238(812)	239(814)	240(816)
241(819)	242(820)	243(821)	244(822)	245(823)	246(824)	247(825)	248(826)	249(827)	250(828)
251(829)	252(830)	253(831)	254(832)	255(833)	256(834)	257(835)	258(836)	259(838)	260(839)
261(840)	262(842)	263(843)	264(844)	265(845)	266(846)	267(847)	268(848)	269(849)	270(850)
271(851)	272(852)	273(853)	274(854)	275(856)	276(861)	277(862)	278(864)	279(865)	280(866)
281(867)	282(869)	283(871)	284(872)	285(874)	286(876)	287(878)	288(879)	289(880)	290(884)
291(886)	292(887)	293(888)	294(889)	295(890)	296(900)	297(921)	298(924)	299(927)	300(945)
301(991)	302(994)	303(1007)	304(1015)	305(1030)	306(1094)	307(1106)	308(1130)	309(1132)	310(1133)
311(1135)	312(1142)	313(1147)	314(1148)	315(1149)	316(1150)	317(1151)	318(1152)	319(1153)	320(1154)
321(1155)	322(1156)	323(1157)	324(1158)	325(1159)	326(1160)	327(1161)	328(1162)	329(1163)	330(1164)
331(1165)	332(1166)	333(1167)	334(1168)	335(1169)	336(1170)	337(1171)	338(1172)	339(1173)	340(1174)
341(1175)	342(1177)	343(1178)	344(1179)	345(1180)	346(1181)	347(1187)	348(1189)	349(1190)	350(1192)
351(1193)	352(1194)	353(1196)	354(1197)	355(1198)	356(1199)	357(1200)	358(1202)	359(1203)	360(1204)
361(1206)	362(1207)	363(1208)	364(1210)	365(1212)	366(1214)	367(1215)	368(1217)	369(1218)	370(1220)
371(1222)	372(1224)	373(1226)	374(1228)	375(1229)	376(1231)	377(1232)	378(1234)	379(1235)	380(1236)
381(1237)	382(1238)	383(1239)	384(1241)	385(1242)	386(1243)	387(1244)	388(1245)	389(1247)	390(1250)
391(1270)	392(1271)	393(1282)	394(1285)	395(1288)	396(1290)	397(1293)	398(1298)	399(1301)	

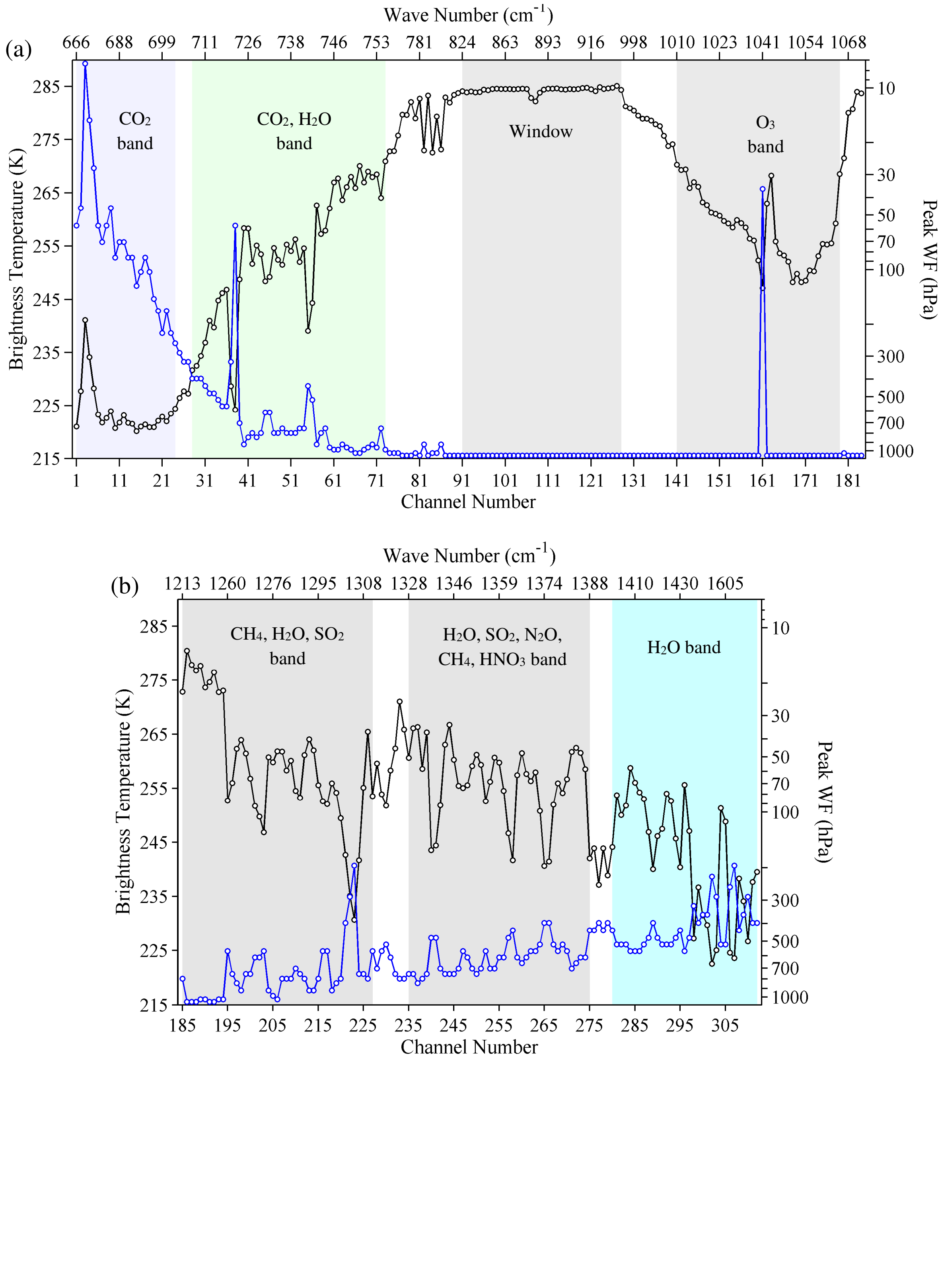

(a)
Wave Number (cm-1)
666 688 699 711 726 738 746 753 781 824 863 893 916 998 1010 1023 1041 1054 1068
CO2 band
CO2, H2O band
Window
O3 band
Brightness Temperature (K)
Peak WF (hPa)
Channel Number
(b)
Wave Number (cm-1)
1213 1260 1276 1295 1308 1328 1346 1359 1374 1388 1410 1430 1605
CH4, H2O, SO2 band
H2O, SO2, N2O, CH4, HNO3 band
H2O band
Brightness Temperature (K)
Peak WF (hPa)
Channel Number

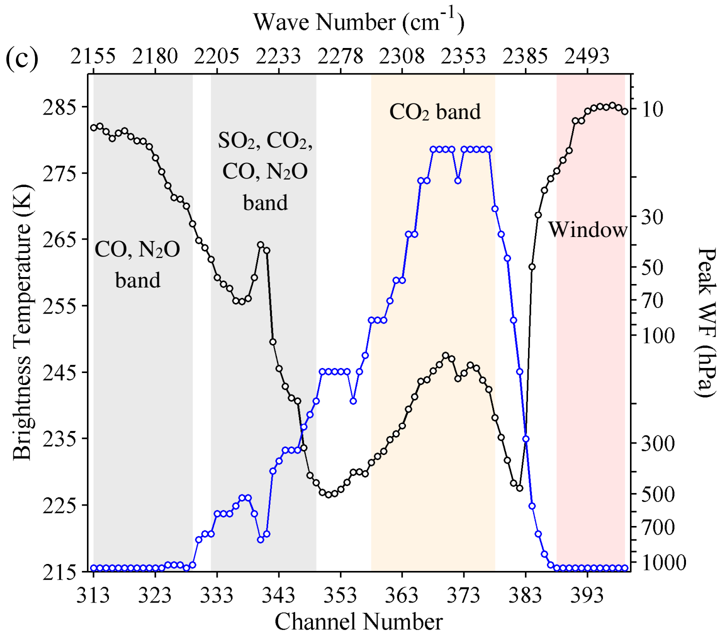

Fig. 1: Brightness temperatures (black) and weighting function peaks (blue) for (a) LWIR, (b) MWIR, (c) SWIR of the 399 CrIS channels used in NWP calculated by CRTM for a typical tropical atmosphere profile. The CO_2 channels of LWIR, CO_2/H_2O channels of LWIR, H_2O channels of MWIR, CO_2 channels of SWIR and window channels of SWIR are represented by purple, green, cyan, orange and red shaded regions, respectively. Other sensitive bands are indicated by grey regions.

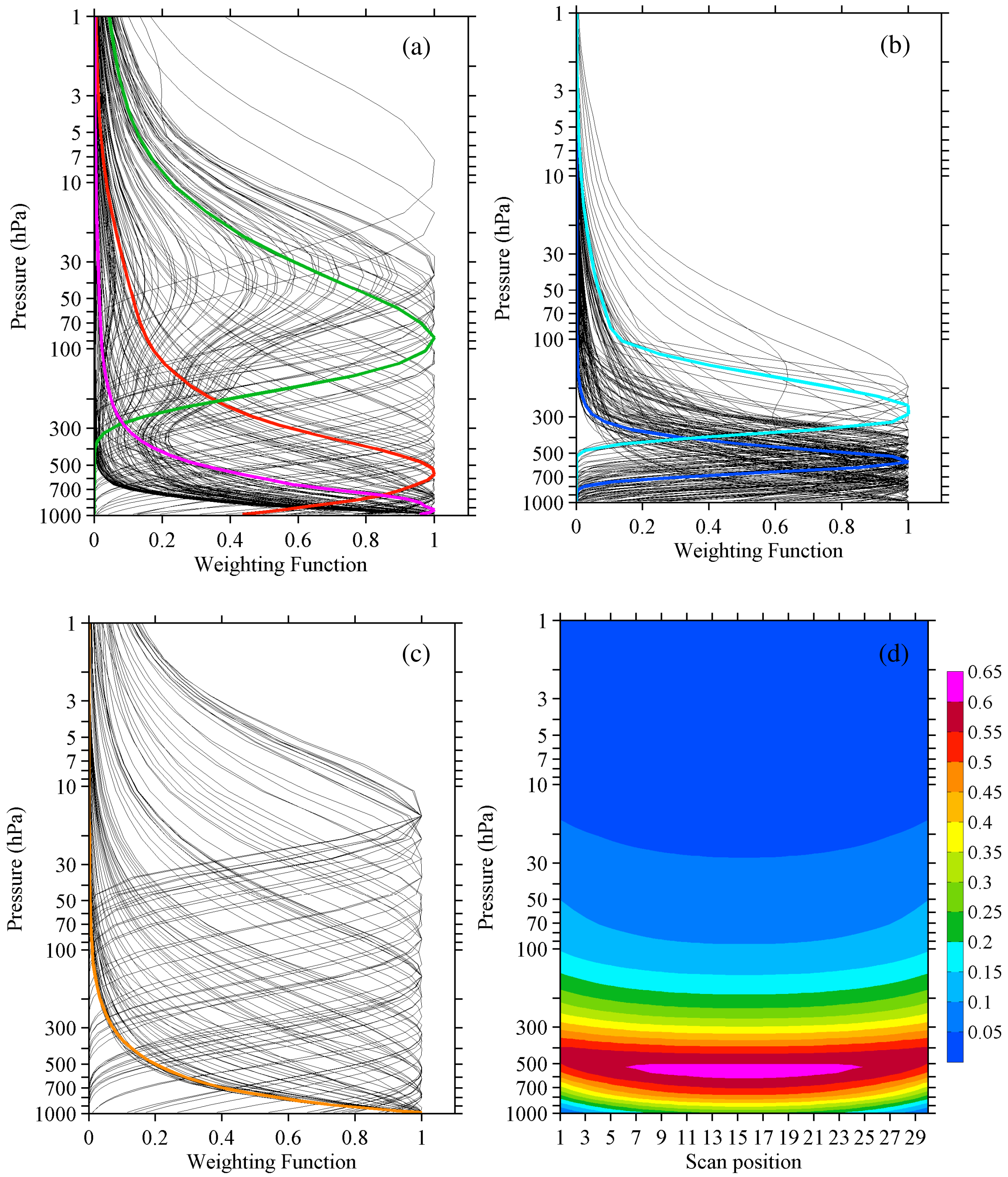

Fig. 2: Normalized weighting functions for bands of: (a) LWIR, (b) MWIR and (c) SWIR. (d) Weighting functions with respect to scan positions and pressure for channel 36. The green, red, purple, blue, cyan, and orange lines in (a), (b) and (c) indicate the LWIR channels 13, 36 and 70, MWIR channels 296 and 303, and SWIR channel 394, respectively.

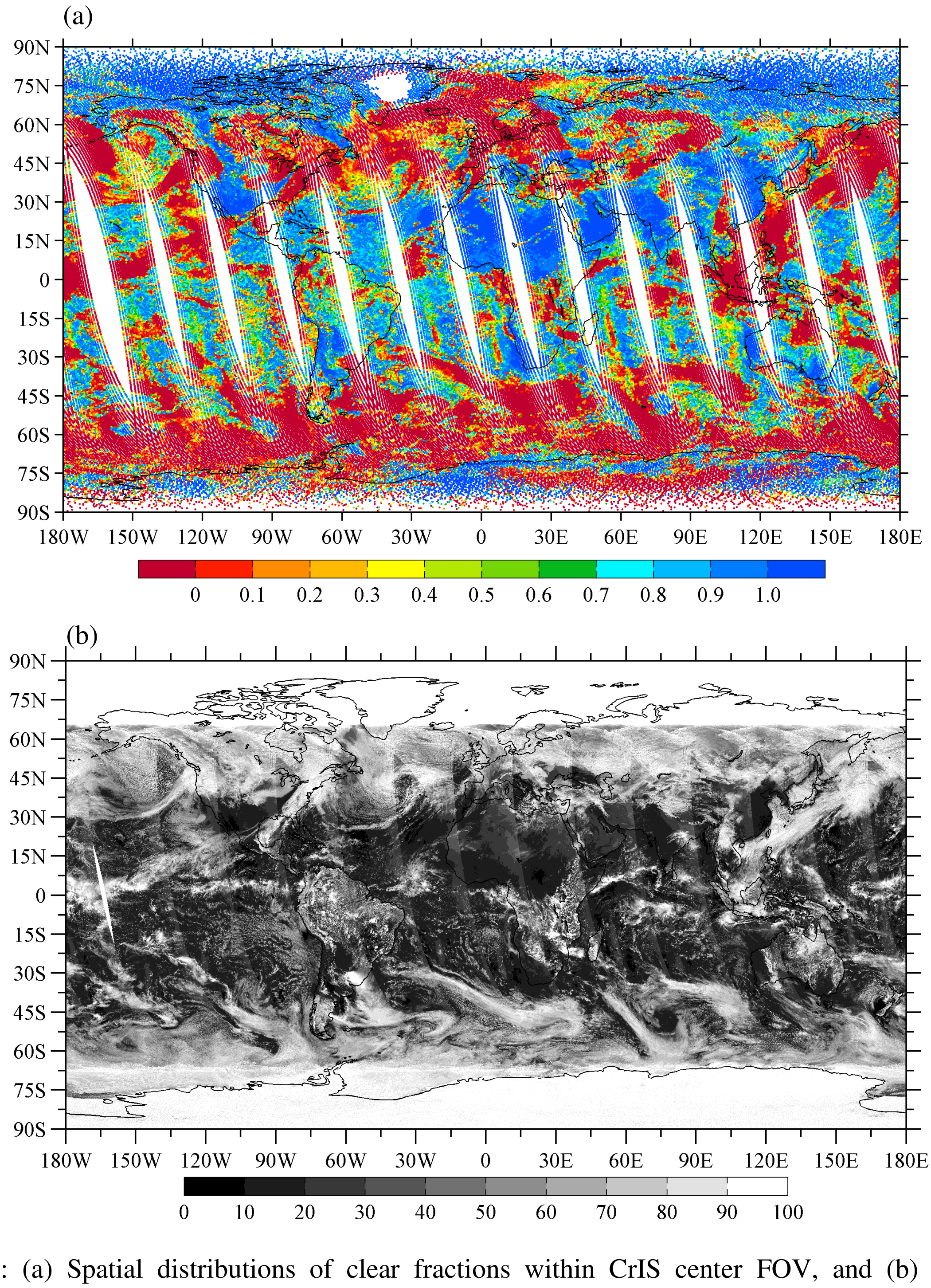

Fig. 3: (a) Spatial distributions of clear fractions within CrIS center FOV, and (b) VIIRS reflectance observations at the M3 visible band centered at wavelength 0.486 μm on 17 December 2015.

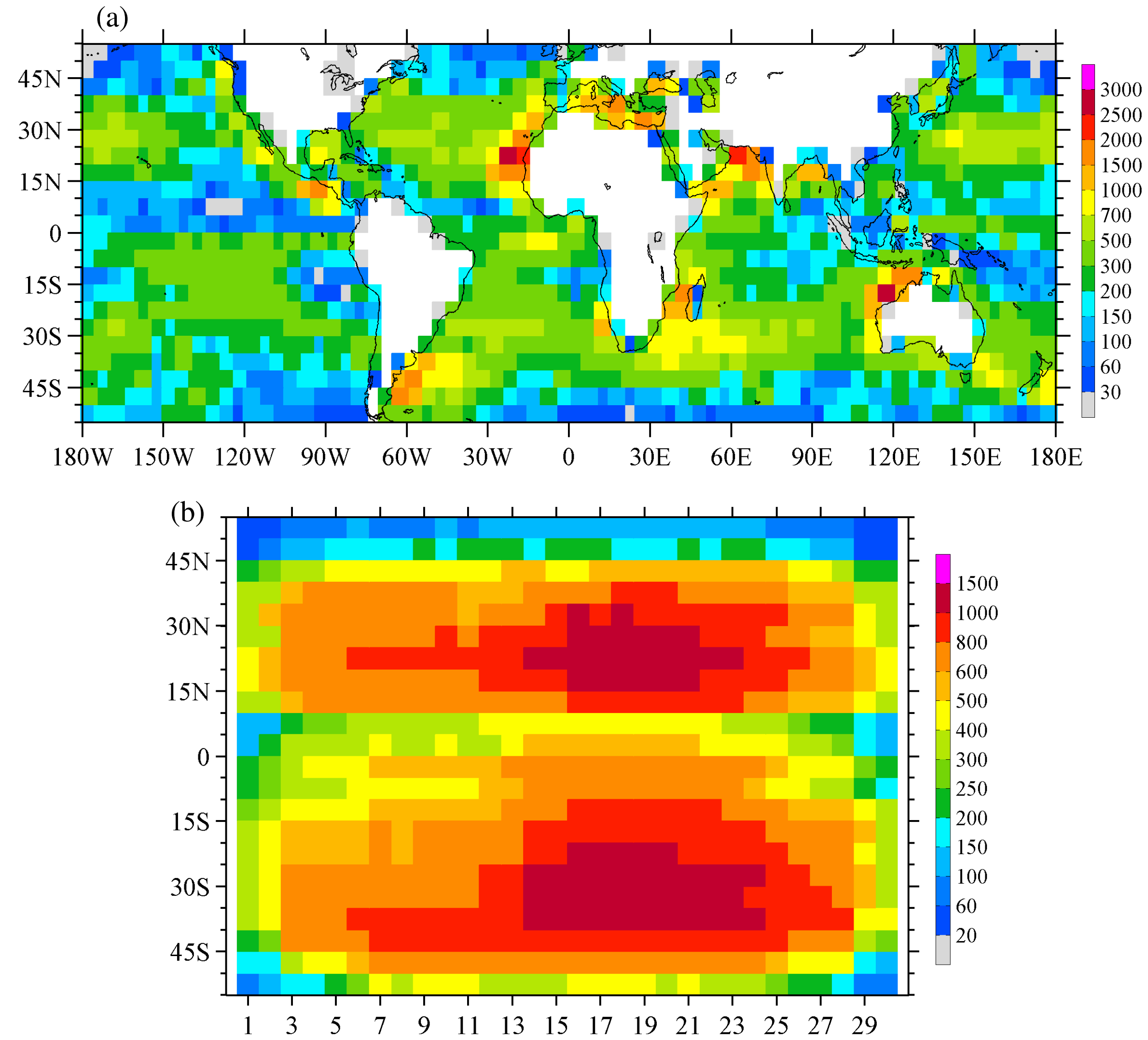

Fig. 4: (a) Global distributions of clear-sky oceanic data counts within 5°x5° grid boxes and (b) the data counts with respect to latitude and scan positions. The data with surface skin temperature below 273.15 K are excluded.

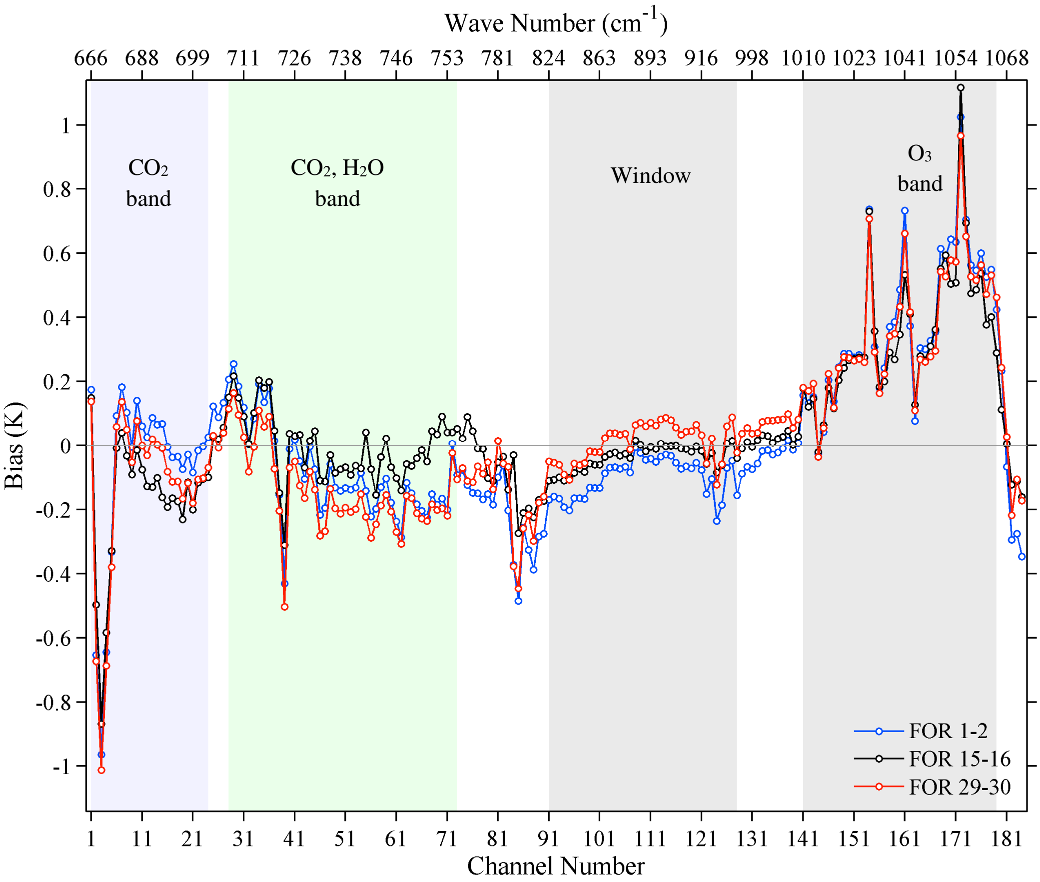

Fig. 5: The biases of brightness temperatures of LWIR channels for FORs 1-2 (blue line), FORs 15-16 (black line) and FORs 29-30 (red line).

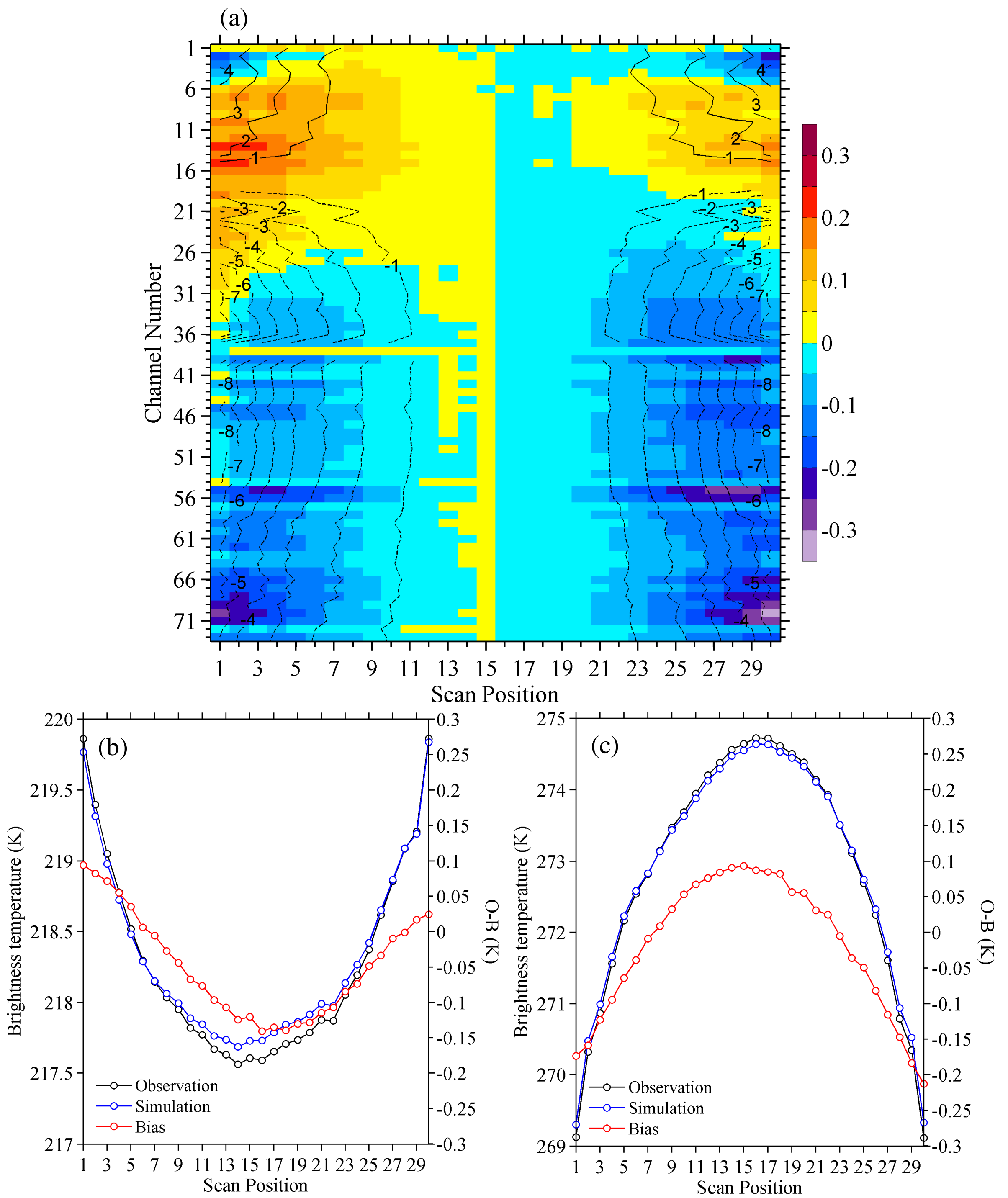

Fig. 6: (a) Scan biases of brightness temperatures for LWIR channels of CO_2 and H_2O absorption band averaged within 55S-55N. The nadir (FORs 15-16) bias is subtracted. The scan variations of mean observed brightness temperatures are shown (contours), with the mean brightness temperatures of FORs 15-16 subtracted. Scan variations of the mean brightness temperatures from observations (black curve) and model simulations (blue

curve) and the O-B differences (red curve) for (b) LWIR channel 13 (689.375 cm^{-1}) and (c) channel 70 (752.5 cm^{-1}).

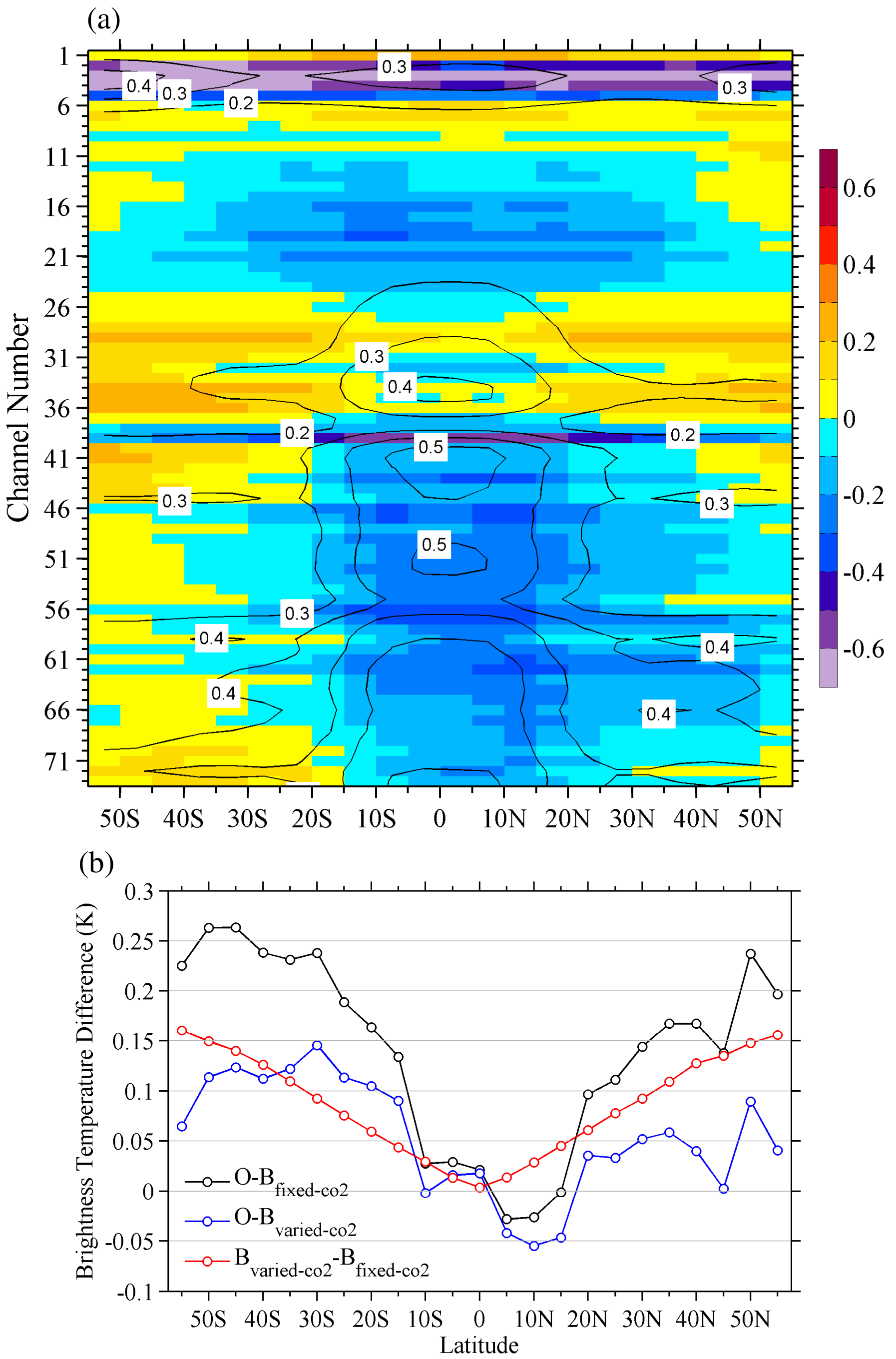

Fig. 7: Latitudinal dependences of biases and standard deviations of the O-B brightness temperature differences for LWIR channels of CO_2 and H_2O absorption bands with respect to latitude and channel number. (b) Latitudinal variations of the O-B differences (unit: K) for LWIR channel 36 (716.25 cm^{-1}) between the fixed CO_2 experiment (black curve) and a latitudinal varied CO_2 experiment (blue curve), and the $B_{varied\text{-}co2}$-$B_{fixed\text{-}co2}$ differences (red curve) with ($B_{varied\text{-}co2}$) and without ($B_{fixed\text{-}co2}$) varying CO_2 concentration with respect to latitudes.

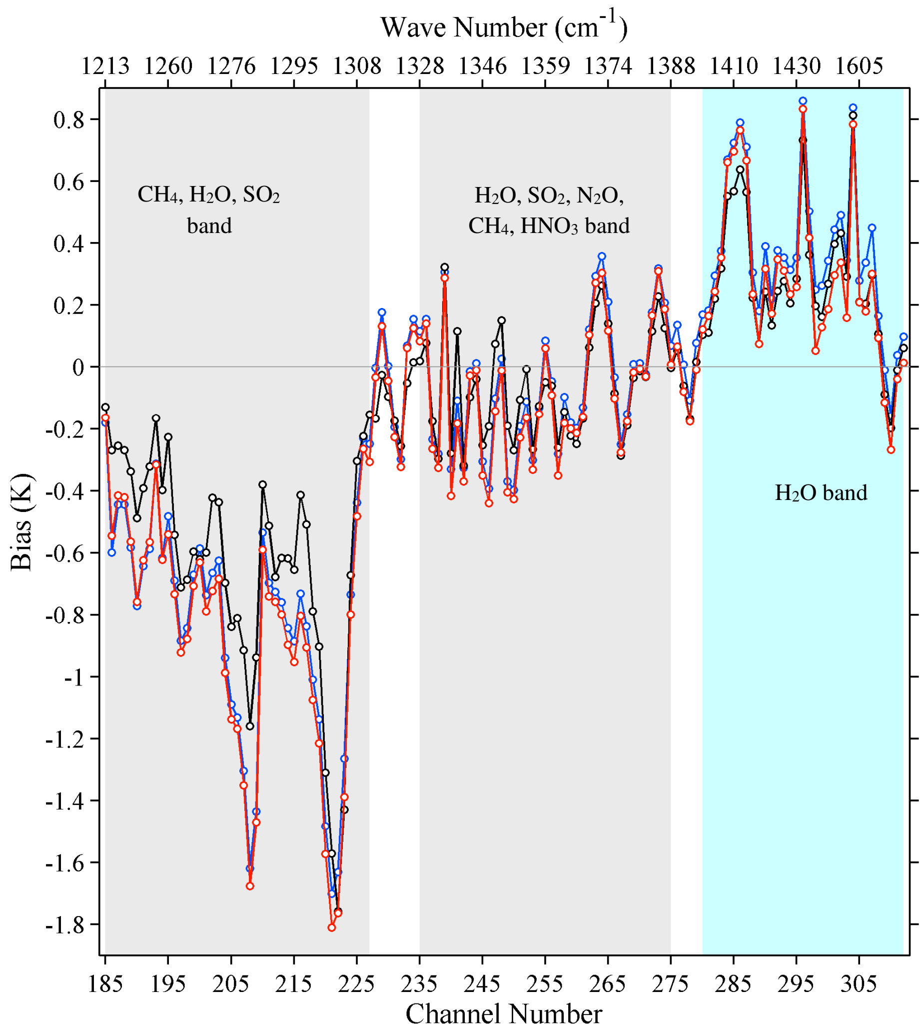

Fig. 8: The biases of brightness temperatures of MWIR channels for FORs 1-2 (blue line), FORs 15-16 (black line) and FORs 29-30 (red line).

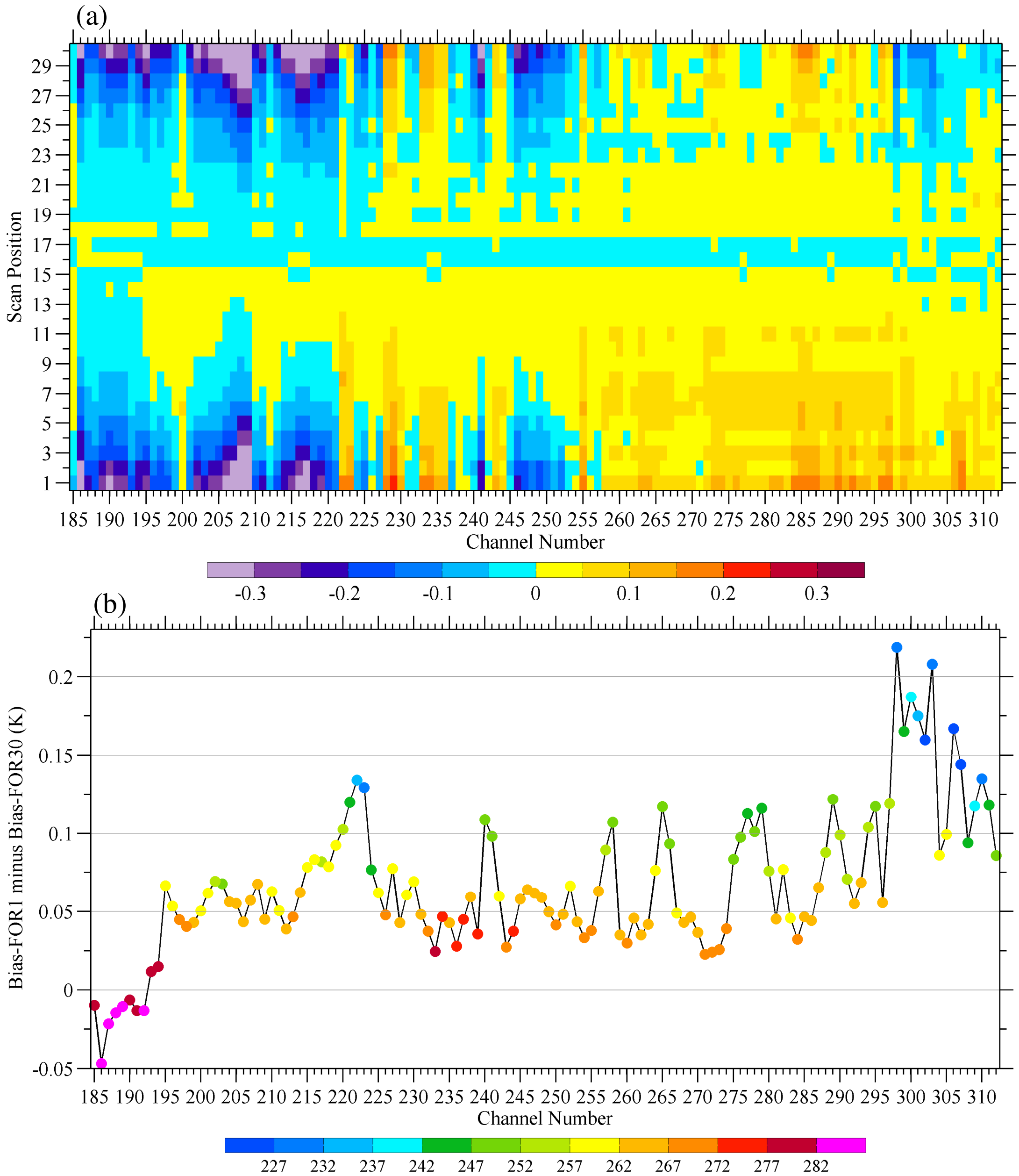
(a)
Scan Position
1 3 5 7 9 11 13 15 17 19 21 23 25 27 29
185 190 195 200 205 210 215 220 225 230 235 240 245 250 255 260 265 270 275 280 285 290 295 300 305 310
Channel Number
-0.3 -0.2 -0.1 0 0.1 0.2 0.3
(b)
Bias-FOR1 minus Bias-FOR30 (K)
-0.05 0 0.05 0.1 0.15 0.2
185 190 195 200 205 210 215 220 225 230 235 240 245 250 255 260 265 270 275 280 285 290 295 300 305 310
Channel Number
227 232 237 242 247 252 257 262 267 272 277 282

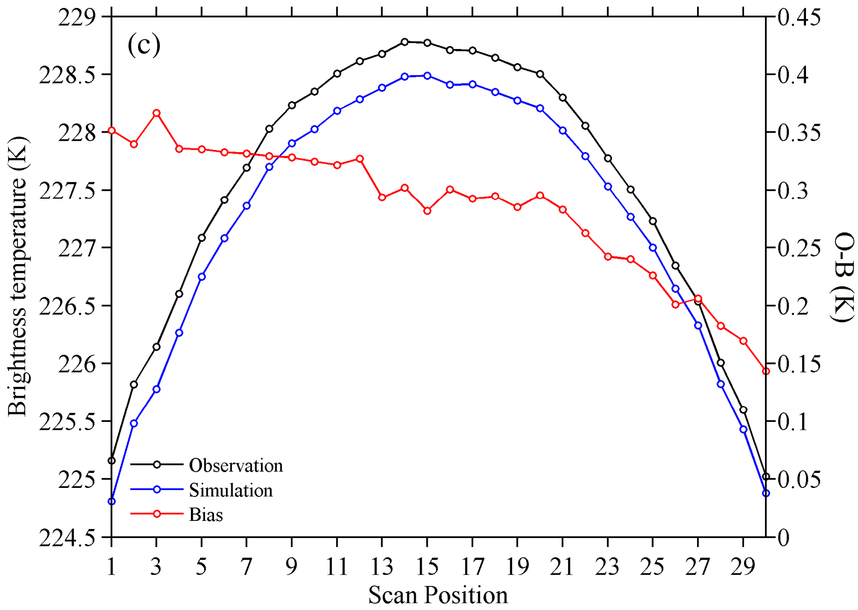

Fig. 9: (a) Scan variations of biases of brightness temperatures for MWIR channels within 55S-55N and (b) the mean differences of biases between FORs 1 and 30 (FOR 1 minus FOR 30) for MWIR channels 185-312 (dots). The nadir (FORs 15-16) bias is subtracted in (a). The mean values of the brightness temperature observations are indicated by colored the dots in (b). (c) Scan variations of the mean brightness temperatures from observations (black curve) and model simulations (blue curve) and the differences (red curve) for MWIR channel 303 (1576.25 cm^{-1}).

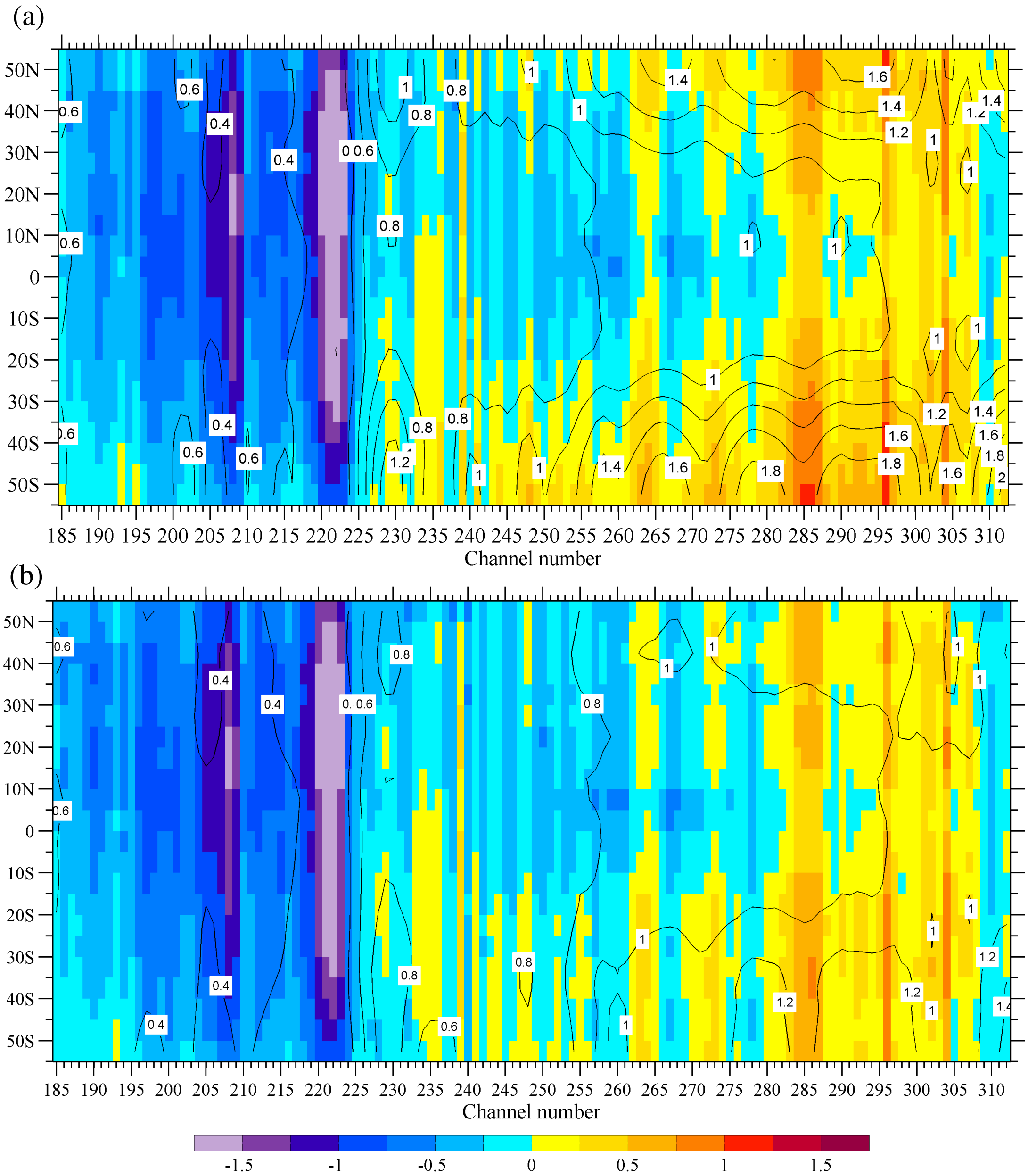

Fig. 10: Latitudinal dependences of biases and standard deviations of the O-B brightness temperature differences for MWIR channels 185-312 with a collocation criteria of (a) ± 3 h and (b) ±1 h.

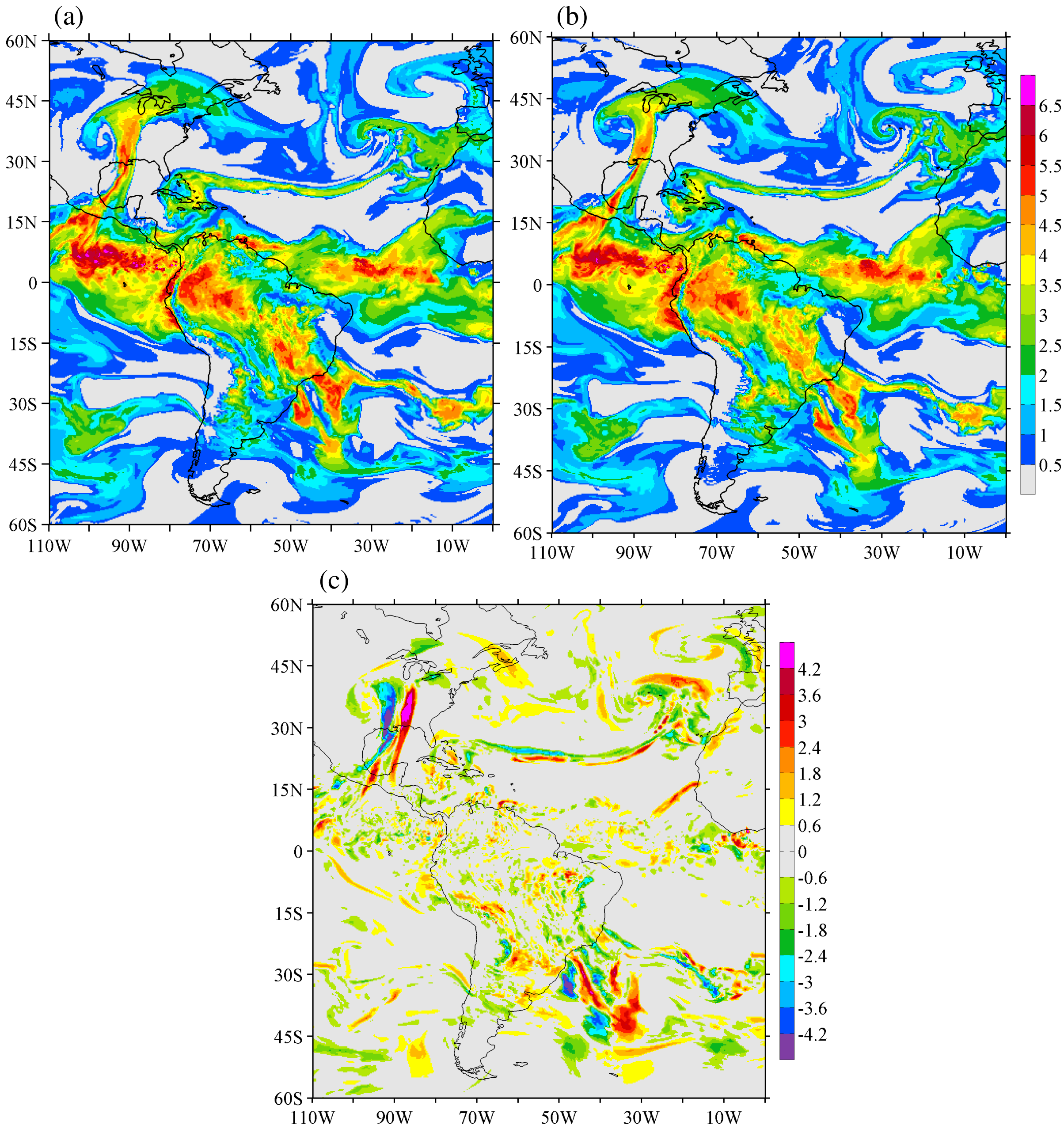

Fig. 11: Specific humidity (unit: g kg^{-1}) around 500 hPa from ECMWF analysis at (a) 0300 and (b) 0900 UTC, 14 December 2015, and (c) their differences.

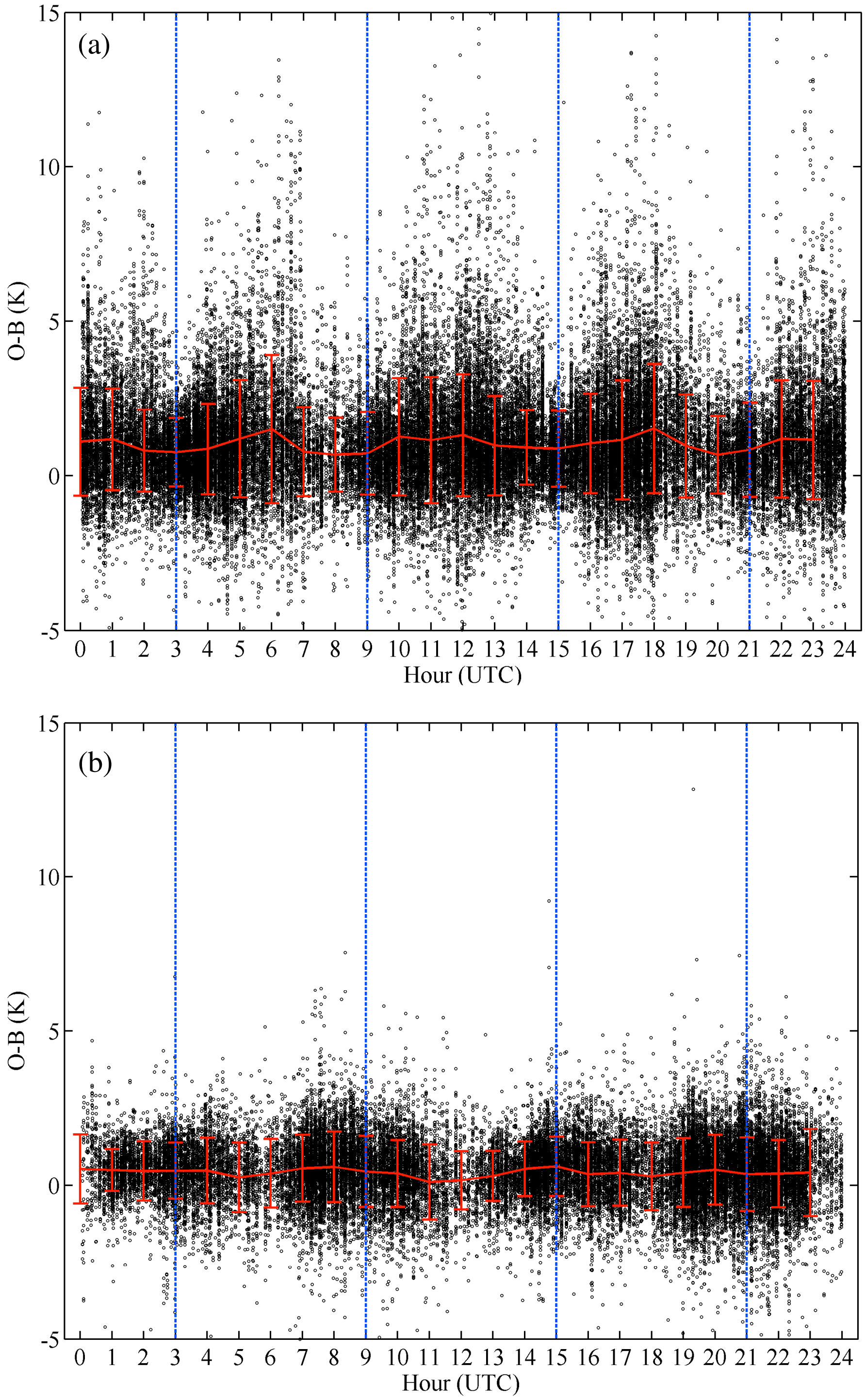

Fig. 12: Scatter plots of O-B of MWIR channel 296 (1442.5 cm^{-1}) for all the data in December within the latitudinal bands of (a) 35N~55N and 35S~55S and (b) 15S-15N. The variations of the bias and standard deviation are presented by red curve and vertical lines, respectively.

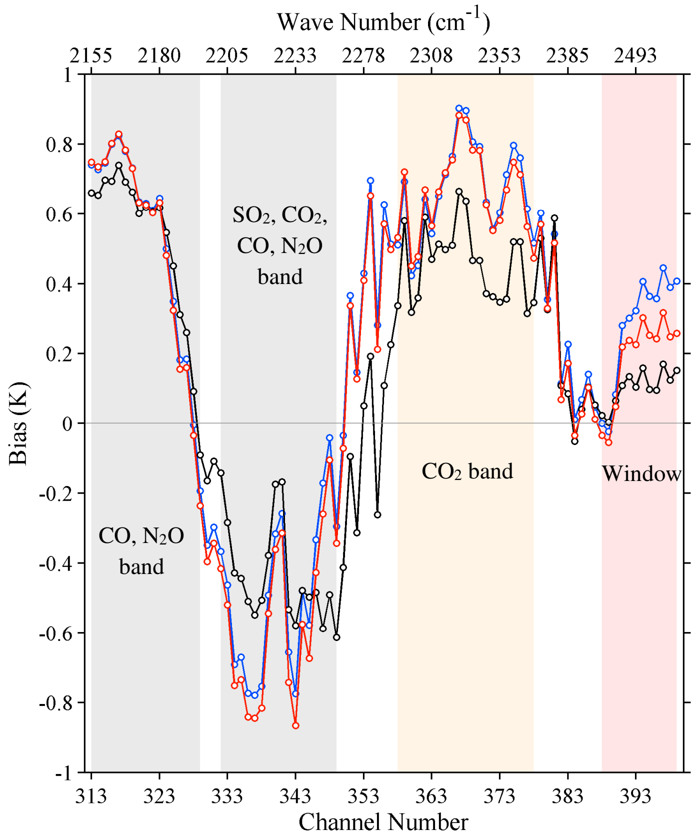

Fig. 13: The biases of brightness temperatures of SWIR channels for FORs 1-2 (blue line), FORs 15-16 (black line) and FORs 29-30 (red line).

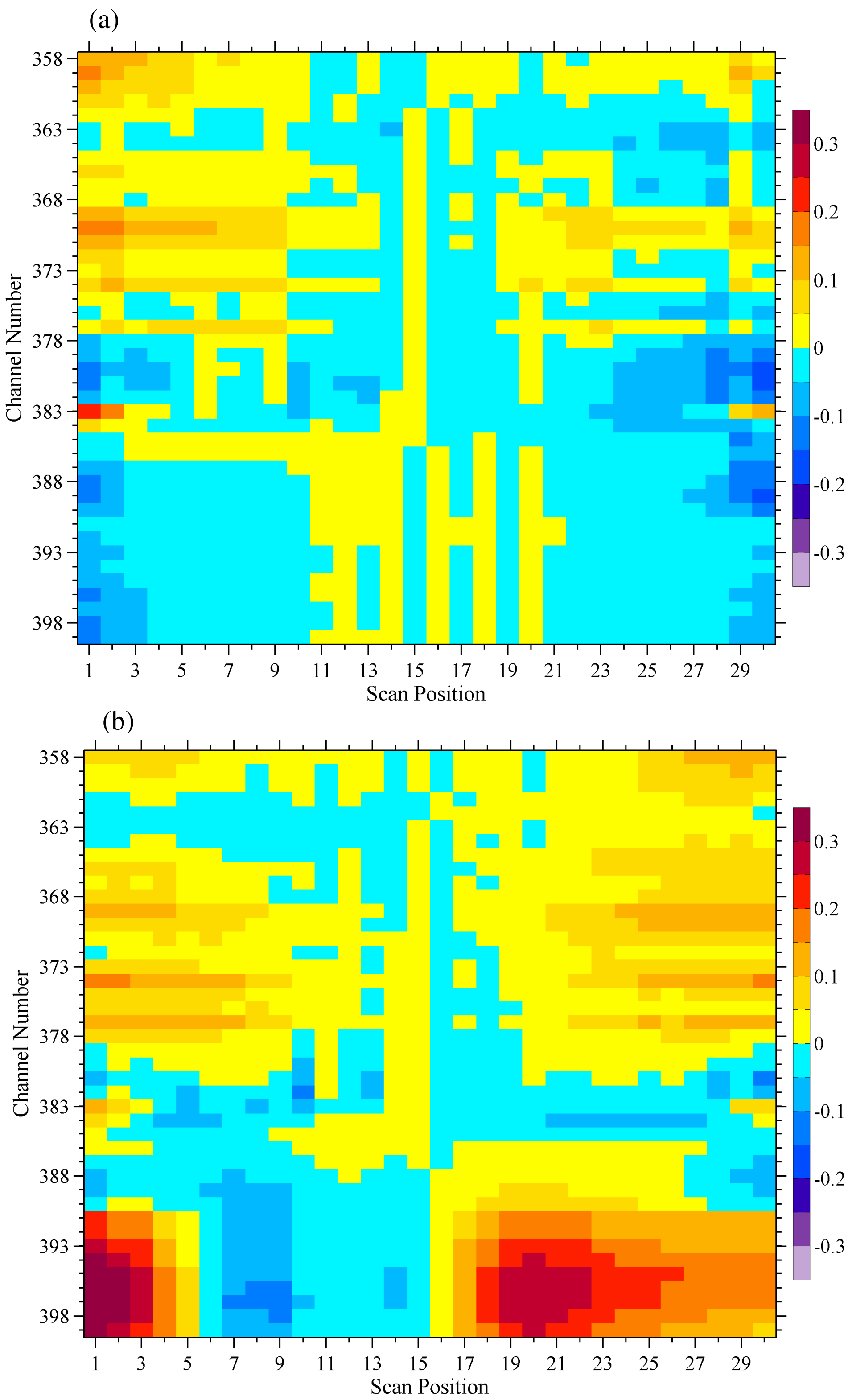

Fig. 14: Biases of brightness temperature for SWIR channels with respect to scan and channel number at (a) nighttime and (b) daytime within the latitudes of 55S-55N. The nadir (FORs 15-16) bias is subtracted.

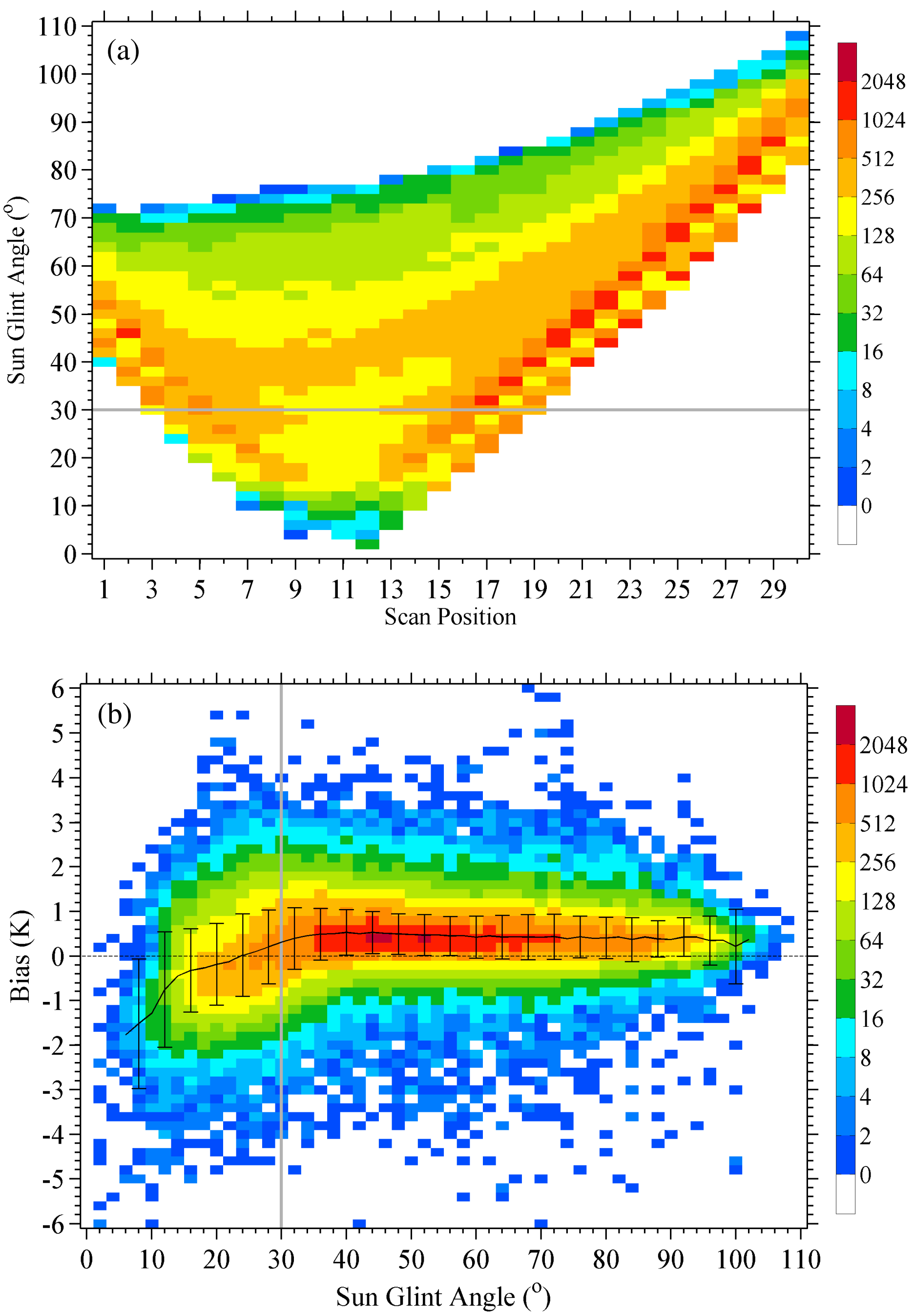

Fig. 15: Data counts (shaded in color) as (a) functions of sun glint angle (intv: 2°) and scan positions and (b) functions of O-B (intv: 0.2 K) and sun glint angle (intv: 2°) of SWIR channel 394 (2500 cm^{-1}) within the latitudes of 55S-55N at daytime. Variations of the global mean biases and the standard deviations with respect to sun glint angle are shown by black curve and vertical lines, respectively. The sun glint angle of 30° is indicated by a grey line in both (a) and (b).

(a) July daytime

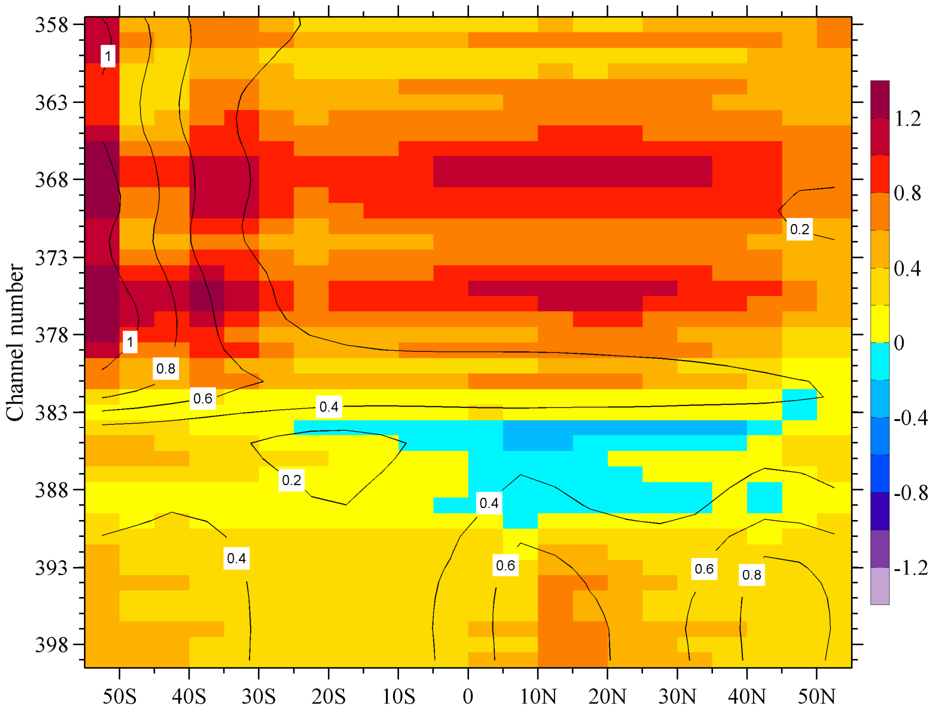

(b) July nighttime

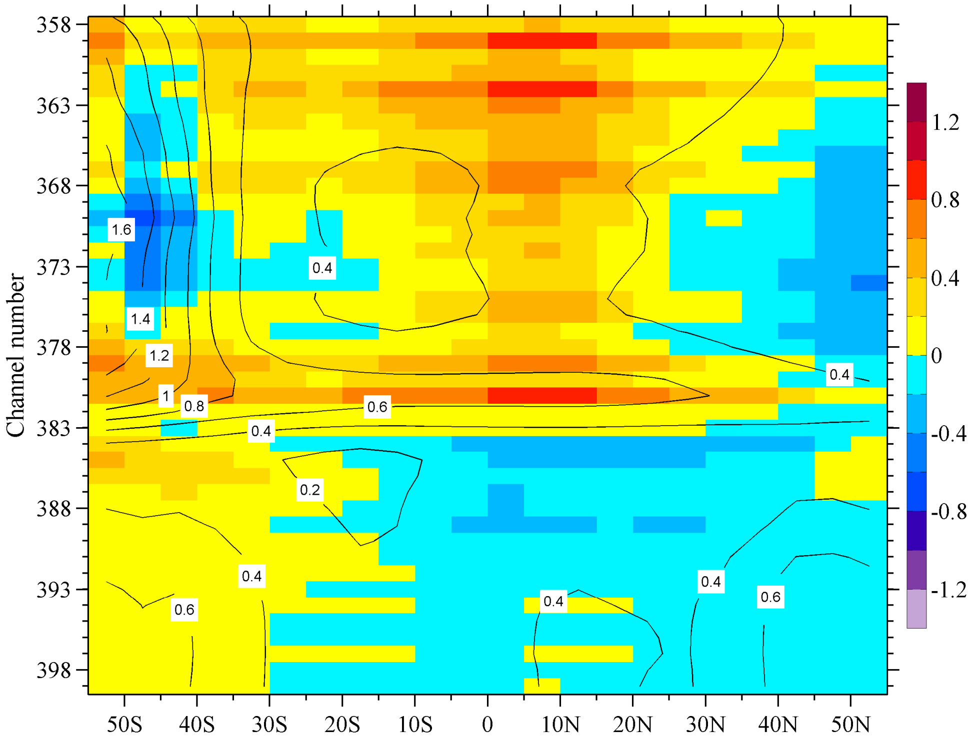

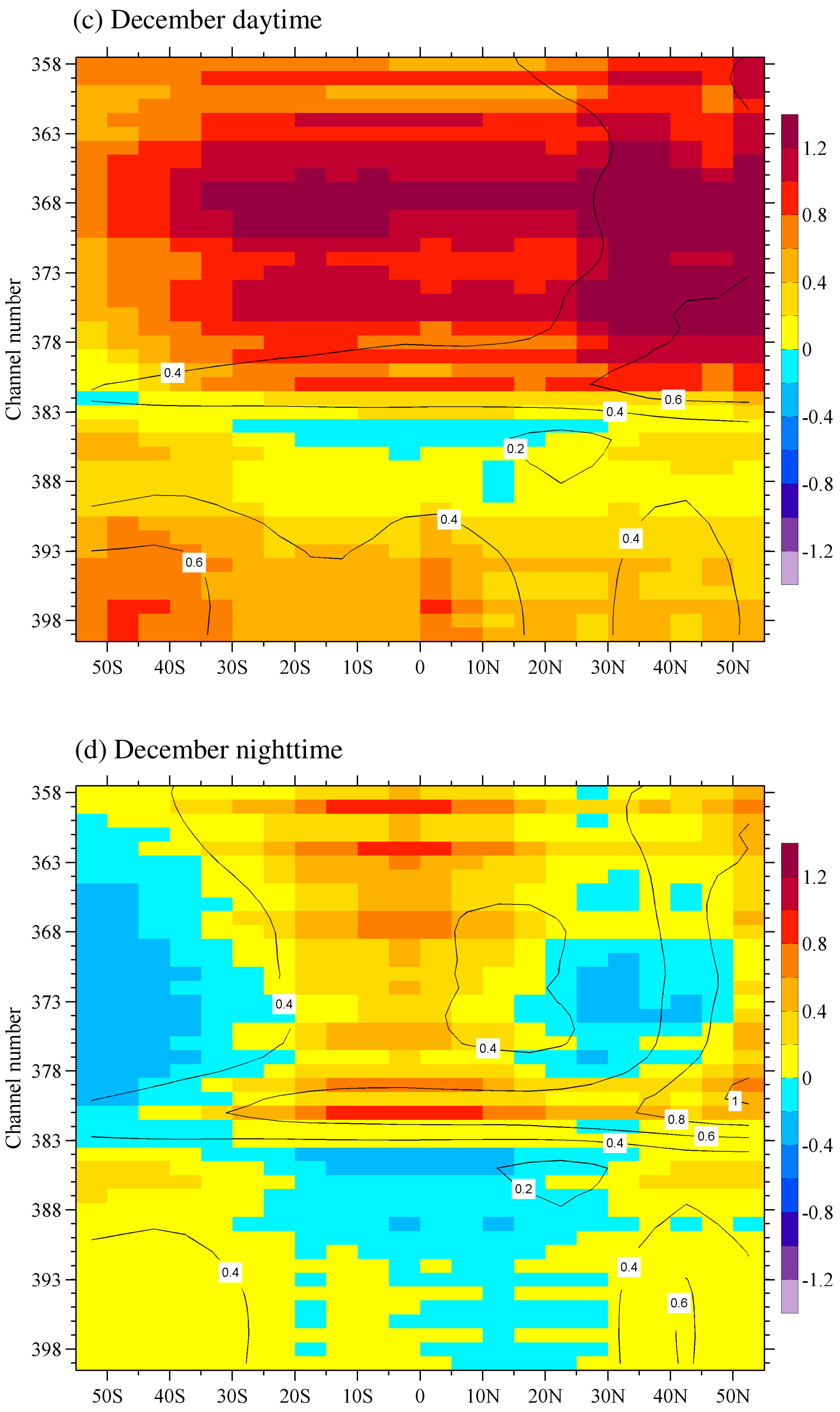

Fig. 16: Latitudinal dependences of biases and standard deviations of the O-B brightness temperature differences for SWIR channels in July during (a) daytime and (b) nighttime, and in December during (c) daytime and (d) nighttime.

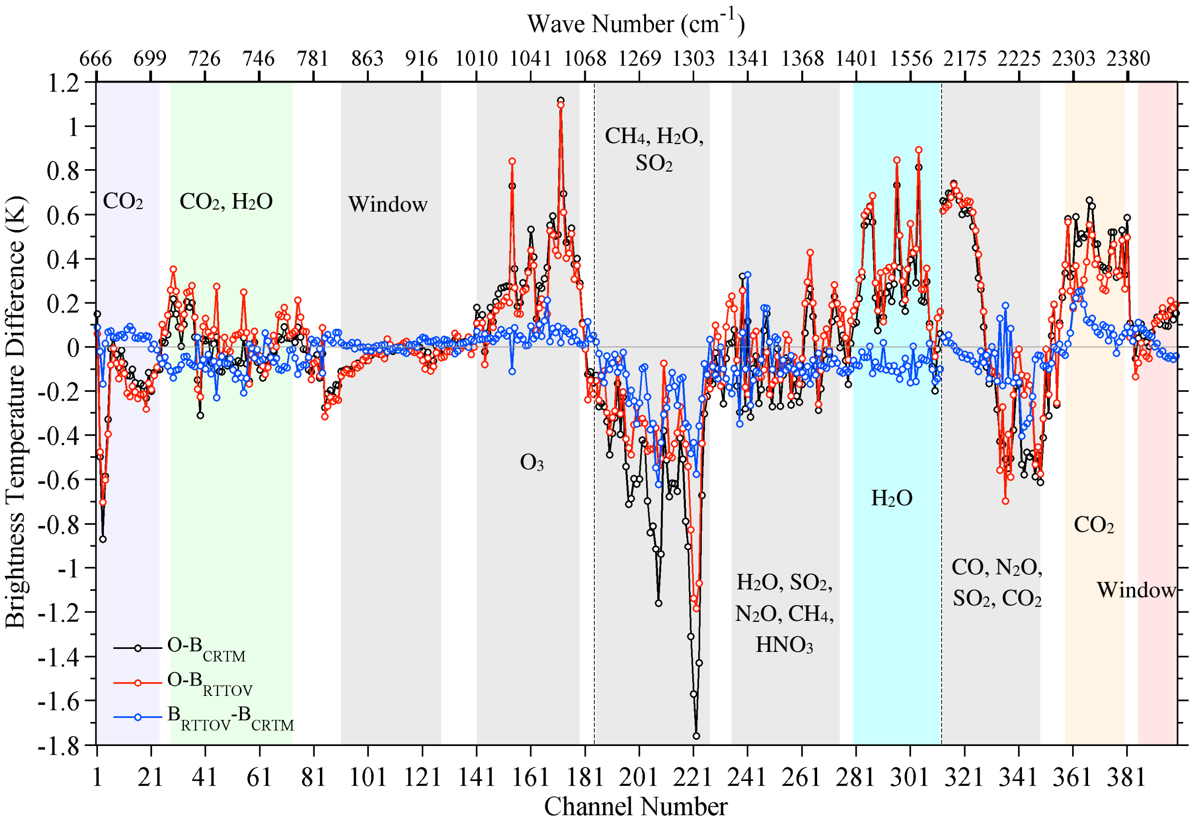

Fig. 17: Biases of CrIS brightness temperatures estimated by CRTM (black, same as Figs. 5, 8 and 13) and RTTOV (red), and differences of bias between CRTM and RTTOV (blue) for the 399 channels at nadir (FORs 15-16). The CO_2 channels of LWIR, CO_2/H_2O channels of LWIR, H_2O channels of MWIR, CO_2 channels of SWIR and window channels of SWIR are indicated by purple, green, cyan, orange and red shadings, respectively. The channels sensitive to other trace gases are highlighted in grey shading.

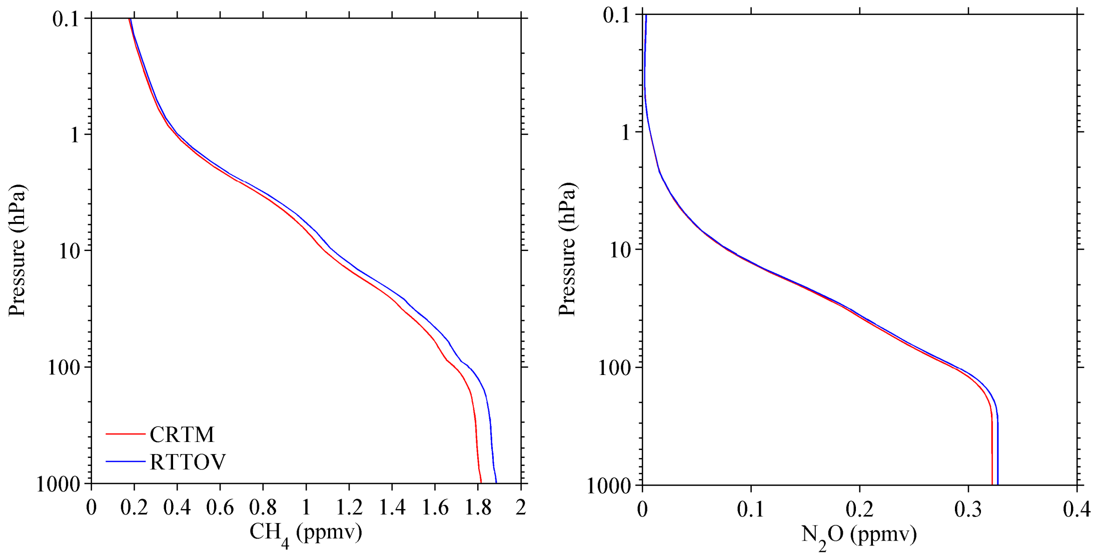

Fig. 18: Reference profiles of CH_4 (left panel) and N_2O (right panel) concentrations within CRTM (red curve) and RTTOV (blue curve).

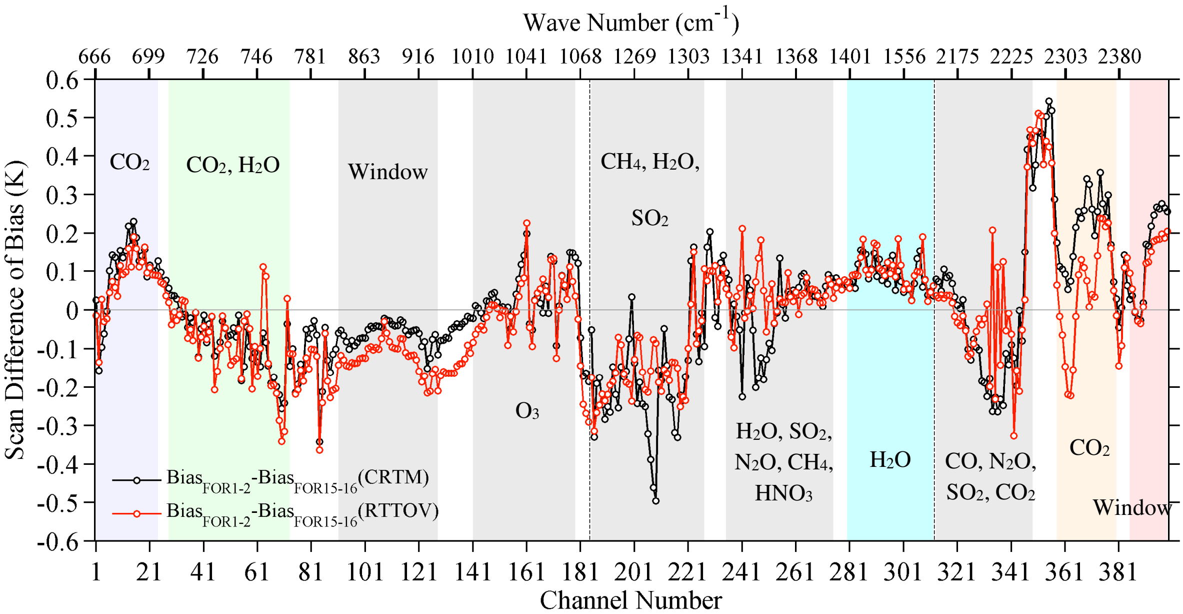

Fig. 19: Mean differences of biases between FORs 1-2 and FORs 15-16 (FORs 1-2 minus FORs 15-16) estimated by CRTM (black) and RTTOV (red).